Doctoral Thesis

Effectively enhanced vibration modes via anharmonic frequency light field

Min Choi

Department of Chemistry

Ulsan National Institute of Science and Technology

2021

Effectively enhanced vibration modes via anharmonic frequency light field

Min Choi

Department of Chemistry

Ulsan National Institute of Science and Technology

Effectively enhanced vibration modes via anharmonic frequency light field

A thesis/dissertation submitted to
Ulsan National Institute of Science and Technology
in partial fulfillment of the
requirements for the degree of
Doctor of Philosophy

Min Choi

06 / 17 / 2021 of submission

Approved by

Advisor
Noejung Park

Effectively enhanced vibration modes via anharmonic frequency light field

Min Choi

This certifies that the thesis/dissertation of Min Choi is approved.

06/17/2021 of submission

signature

Advisor: Noejung Park

signature

Jun Hee Lee: Thesis Committee Member #1

signature

Hyeong-Ryeol Park: Thesis Committee Member #2

signature

Geunsik Lee: Thesis Committee Member #3

signature

Hyun Woo Kim: Thesis Committee Member #4;

Abstract

The Walter Kohn and Lu Jeu Sham's representation of density functional theory, called Kohn-Sham equation, is especially advantageous to the various hierarchical theoretical methods in the condensed material field because of its simplicity and practicality. The Kohn-Sham equation is aim to the investigation of the electronic structure of materials based on a first-principle perspective without advanced inputs derived from prior knowledge.

This thesis deals with the applications of the Kohn-Sham density functional calculation in electrochemical catalyst and the motion of molecules. Using the computational source, thermodynamical treatments, and the real-time dynamics in alternative current field were researched. The first and second parts are regarding the electrochemical reactions, hydrogen evolution reaction and oxygen reduction reaction. The introduction and several case studies for hydrogen evolution and oxygen reduction reaction are handled with published papers. The third section introduces the importance of anharmonicity of molecular vibration for methane case study. The concept of group velocity and group temperature for molecular dynamics and the development of multi-frequency vector potential light field are presented. The anharmonicity is influenced to elongate the molecular bond effectively. Beyond the harmonic regime, anharmonic frequency obtained from the potential energy surface is helpful to enhance the vibration modes effectively.

Content

List of Figures

List of Tables

I. Introduction

Mathematical formulations of natural laws have been chased ultimately established theory since Isaac Newton released the equation of motion for the classical matters. The physical laws of dynamics represented in uncomplicated mathematical formula have been used to the prognostication of nature and been applied to a rigid groundwork for various fields of science and technology. At the specific perspective, the observable experimental researches have been inconsistent in that established theory. This inconsistency has led the improvement of theoretical knowledge, especially physics, and enabled the investigation of innovative laws of universe. In the early 20^{th} century, the difference between theoretical perspective and experimental observations brought out the necessity of the introduction of quantum physics. [1] The unpredicted observation showed novel physical events in the quantum universe such as particle-wave duality or the indistinguishability of a particle. On the basis of these phenomena, Ervin Schrodinger, Werner Heisenberg, and other trailblazers established the formula for the dynamics of particle in the micro-perspective, or quantum mechanics. It is still difficult to obtain the exact solutions of the indistinguishability of quantum particles for the many-body systems.

To forecast the dynamics of particles based on the Schrodinger equation, diverse approaches have been suggested and proved. Among these manners, Walter Kohn and Lu Jeu Sham suggested that the indistinguishability for a bosonic particle is able to be estimated as a local density functional potential. [2] This effective density functional potential induced the possibility to depict the influence of a many-body system as the single body equations, and it is called Kohn-Sham equation. Founded on the density functional theory (DFT) approach, steady-state characteristics of various matters have been investigated theoretically such as the geometric configurations, electronic band structure, and magnetization properties. To investigate the real-time dynamics of electronic configuration beyond the steady-state, the wavefunction time-propagation of the electron of material also has been researched by the time-dependent DFT (TDDFT) method and the time-propagated profile of observable properties estimated by time-propagated wavefunctions compared with the experimental outcomes. [3, 4]

In this thesis, the brief review of DFT and TDDFT are introduced. Fascinating for the physical phenomena related without and with real-time dynamics are explored in succession. In particular, three different studies in materials and mechanisms are introduced as examples of without and with real-time dynamics. The first and second parts are regarding the electrochemical reactions, hydrogen evolution reaction and oxygen reduction reaction. The introduction and several case studies for hydrogen evolution and oxygen reduction reaction are handled with published papers. [5-8] The third section introduces the importance of anharmonicity of molecular vibration for methane case study. The concept of group velocity and group temperature for molecular dynamics and the development of

multi-frequency vector potential light field are presented. The anharmonicity is influenced to elongate the molecular bond effectively. Beyond the harmonic regime, anharmonic frequency obtained from the potential energy surface is helpful to enhance the vibration modes effectively. These three studies represent the application of DFT calculation to investigate the catalytic properties and show the advantages of the Ehrenfest dynamics method unable to be interpreted by the stationary electronic structure. It was figured out that the time-dependent profile of the physically observable properties becomes a significant criterion to interpret the real-time dynamics in matters. The real-time dynamics simulated by the TDDFT method are applied to research the time-propagation of electron under the extrinsic perturbations.

II. Theoretical background and computational details

2.1. Density functional theory

2.1.a. Kohn-sham equation

In 1960s, Werner Hohenberg and Walter Kohn reported two remarkable theorems for the calculations of a system consisting of non-interacting particles. [9] The first theorem shows that the electron charge density is nominated by the external treatment. The second theorem is related with the calculated ground-state eigenvalue from the variational principle. Along these two theorems, the effective equation for single body system, called the Kohn-Sham equation, can be introduced to calculate the ground state of many-body system. From the Kohn-Sham equation, the local density functional is used to depict the electron-electron correlation, interaction, and exchange. The wavefunction of ground electronic state and quasiparticle energy level can be calculated by solving the Kohn-Sham equation. The formula of Kohn-Sham equation can be described as follows

$$\left[-\frac{1}{2}\nabla^2 + V_{ion}(\vec{r}) + V_{Columb}\left[\rho(\vec{r})\right] + V_{XC}\left[\rho(\vec{r})\right]\right]\psi(\vec{r}) = \varepsilon\psi(\vec{r}) \quad (2.1),$$

where V_{ion}, V_{Columb}, and V_{xc} are the potential of ion-ion interaction, electron-ion and electron-electron coulombic interaction, and exchange-correlation for electron-electron interaction, respectively.

In the first state of DFT development, Walter Kohn and Lu Jeu Sham argued that the exchange interactions among the non-interacting electrons in matter can be estimated as an exchange interaction of unvaried electron charge density.

$$V_{XC}^{electron-gas}\left[\rho(\vec{r})\right] = 3\pi/4\rho(\vec{r}) \quad (2.2)$$

Even though the exact many body interactions among the indistinguishable electrons are not able to be figured out, the Walter Kohn and Lu Jeu Sham's suggestion made it possible to depict the electronic structures of various materials. After their suggestion, the enhanced exchange functional has been developed for more accurate representation of electronic system. The local density approximation (LDA) depicts the expression of exchange interaction of unvaried electron charge density and extra correlation to make up for the skipped parts compared to the many-body interaction. [10] Additionally, the spin part of an electron in a specific system can be considered by allocating two distinguished states. As a result, the stationary features of a materials such as lattice parameter or band gap can be measured based on the DFT method.

For the enhanced representation of the material characteristics based on the first-principle calculation, a generalized gradient approximation (GGA) method is employed which appends the gradient of the electron charge density based on the LDA expression. [11] There are still obstacles, however, about the description of material characteristics related to the many-body interaction of electrons by calculating the single body equation. For instance, the bandgap obtained by DFT is often in discord

with the experimentally observed optical bandgap. This mismatch is based on the many body effect of excited state. To describe the many body interaction of excited state from the ground-state, Lars Hedin proposed the self-consistent equation named Hedin's cycle. [12] Based on the research, the exact optical bandgap could be calculated by the DFT simulation with the simple correction of the many-body interaction. For instance, the GW approximation handles the two-body interaction between hole and negative carrier effect, and between electron and positive carrier effect. The Bethe-Salpeter equation contains the four-body interaction among hole, electron, negative carrier effect, and positive carrier effect. There were several similar methods to describe the many-body interactions exactly under the first-principle scheme such as the DFT+DMFT method. [13]

2.1.b. Self-consistent field and basis set

These days, a few professional groups mainly develop the computational packages for *ab initio* calculation. Each of them has its own advantages related with numerical calculation and technique. The employed mathematical algorithms can be classified relying on the type of basis set for the description of electronic wavefunction. For instance, the plane-wave (PW) basis set is specialized to represent the 3-dimensional periodic systems, and it is applied in the VASP, Quantum ESPRESSO, and ABINIT source codes.[14-16] The simulation source code based on the PW basis set, however, requires a high computational performance for the Fast Fourier transform (FFT). The basis set using the numerical grid embedded in the OCTOPUS source code can represent the multi-dimensional periodic systems. The basis set using localized atomic orbital is applied in the SIESTA source code, and it requires a low computational cost by using an external numeric algorithm. The basis set using a full-potential linearized augmented plane-wave is embedded in the Wien2k and ELK source code, and it can treat the all-electron wavefunctions by using the augmented core-electron wavefunctions. Even though these basis set have individual calculational issues related with execution, the core algorithm for the DFT simulation is popularized.

The self-consistent algorithm in DFT based on the PW basis set is represented in Figure 2-1. In the first step for the DFT simulation, the Kohn-Sham Hamiltonian for the simulation should be established. System configuration, initial atomic charge density, and basis set for Kohn-Sham states are needed to build the initial Kohn-Sham Hamiltonian. To build the initial atomic charge density, $\rho^{init}(\vec{r}) = \sum_{n}^{occ} \left|\psi_n^{guess}(\vec{r})\right|^2$, arbitrary atomic orbital states, $\psi_n^{guess}(\vec{r})$, are employed. After the establishment of the Kohn-Sham Hamiltonian, the Kohn-Sham wavefunction, $\psi_n^{KS}(\vec{r})$, and Kohn-Sham eigenvalues, ε_n^{KS}, are measured by diagonalizing the matrix. The obtained Kohn-Sham wavefunctions are represented in the instinct basis set. For instance, the Kohn-Sham wavefunction based on the PW basis set can be depicted as follows $\psi_n^{KS}(\vec{r}) = \sum_{\vec{G}}^{E_{cut}} C_n(\vec{G}) e^{i\vec{G}\cdot\vec{r}}$, where E_{cut} is the cutoff energy for the PW. The updated charge density, $\rho^{new}(\vec{r}) = \sum_{n}^{occ} \left|\psi_n^{KS}(\vec{r})\right|^2$, can be obtained using the previous Kohn-Sham wavefunctions. The nonlinearity of the Kohn-Sham equation allows the updated Hamiltonian establishment using the updated charge density to renew the updated Kohn-Sham wavefunction that is different from the formerly obtained one. Kohn-Sham equations, therefore, are iteratively calculated by renewing the Kohn-Sham Hamiltonian from previous state. If the specific criteria such as charge density, total force, or total energy difference are satisfied, the iterative algorithm is concluded. This algorithm is a commonly called self-consistent field (SCF) algorithm in

the DFT simulation. As a result, the Kohn-Sham wavefunctions and eigenvalues of the ground state can be iteratively calculated.

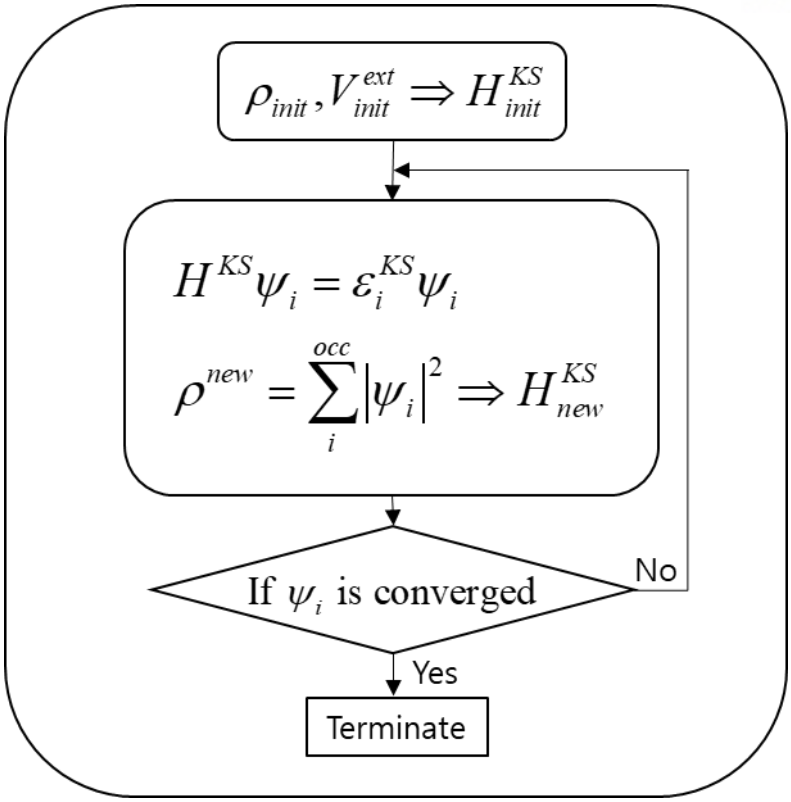

Figure 2-1. Flowchart of self-consistent algorithm for DFT

2.1.c. Pseudopotential

Efficient approximation can importantly decrease the computational costs. Pseudopotential approach is one of instance of an efficient approximation method for the DFT simulation. [17] This approach comes from the brief concept that the core-electrons are bounded in their atomic orbital states though the valence electrons are redistributed by an extrinsic perturbation. The valence electron in the Kohn-Sham Hamiltonian are based on this assumption. The additional potential, or pseudopotential, term is used to make up for the interactions between valence electron states and core-electron states. All-electron wavefunctions for a monoatomic system calculated by DFT simulation are needed to generate the pseudopotential as follows:

$$\left[-\frac{1}{2}\frac{d^2}{dr^2}+\frac{l(l+1)}{2r^2}-\frac{Z}{r}+\int\frac{\rho(r')}{|r-r'|}dr'+\mu_{xc}[\rho]\right]rR_{nl}^{AE}(r)=\varepsilon rR_{nl}^{AE}(r) \quad . (2\text{-}3)$$

with all-electron wavefunctions, pseudo-wavefunctions and pseudo-potentials can be measured. Only the radial term of the wavefunction can be considered by the spherical symmetry in a monoatomic system. The measured pseudo-wavefunctions should fulfill some criterions compared to the all-electron Kohn-Sham wavefunctions as follows:

$$\begin{aligned}&\left[-\frac{1}{2}\frac{d^2}{dr^2}+\frac{l(l+1)}{2r^2}+V_{l,sc}^{PP}(r)\right]rR_{nl}^{PS}(r)=\varepsilon_l rR_{nl}^{PS}(r),\\&V_{l,sc}^{PP}(r)=\varepsilon_l-\frac{l(l+1)}{2r^2}+\frac{1}{2rR_l^{PS}}\frac{d^2}{dr^2}\left[rR_l^{PS}(r)\right]\end{aligned} \quad (2\text{-}4)$$

Consequently, the pseudo-potential for an allowed total angular momentum is represented by:

$$\begin{aligned}&V_l^{PP}(r)=V_{l,sc}^{PP}(r)-\int\frac{\rho_v(r')}{|r-r'|}dr'-\mu_{xc}[\rho_v],\\&\rho_v(r)=\sum_{l=0}^{l_{\max}}\sum_{m=-l}^{l}\left|rR_l^{PS}(r)\right|^2\end{aligned} \quad (2\text{-}5)$$

In the Kohn-Sham Hamiltonian, the pseudo-potential in Eq. 2-5 is substituted the all-electron potential.

2.1.d. Electrochemical profile in DFT

The DFT simulation can provide the theoretical perspective in catalyst field, especially oxygen reduction reaction (ORR) and hydrogen evolution reaction (HER). The computational results by the DFT is corresponding to the experimental observations. Both of ORR and HER are dealt with and corrected by thermodynamical treatments. Priorly, the ORR mechanism has various reaction paths schematically represented in Figure 2-2 and reaction conditions such as pH, temperature, or pressure. There are two different paths, association and dissociation, in ORR. In the ORR process, the simulated thermodynamical energies of molecules are assumed as gas phase, though the phase of target molecules, especially water molecule, in the real experimental situation are mostly liquid phase. The energy for the liquid phase of the water molecules is treated as follows:

$$E_{H_2O(l)} = E_{H_2O(g)} + RT\ln(p/p_0), \text{ (2-6)}$$

where R, T, p, and p0 indicate ideal gas constant, temperature, pressure, and vapor pressure, respectively. The energy for the aqueous phase of the proton ion based on thermodynamics is obtained based on Nernst equation as follows:

$$E_{H^+(aq)} = \frac{1}{2}E_{H_2(g)} - RT\ln 10 \times \mathrm{pH}, \text{ (2-7)}$$

where pH is proton concentration. The proton source substitutes proton ion for water if the solution is alkaline condition. For the poisoning problem, the formation energy for hydroperoxide, called two-electron process, should be compared to that for water, called four-electron process. The oxygen adsorption and dissociation barrier are also needed to be calculated by nudged elastic band method to prove that material is available for ORR catalyst. [18, 19] The formation energy for each reaction step is comparable to the experimental results. The overpotential in experiment represents the required energy to make downhill in formation energy profile. When the potential $U = U_0 - n\eta$, where n is number of electron and η is overpotential, makes downhill, there is no barrier for reaction step, and the current starts to flow. The corresponding overpotential can be determined in the i-V curve. To analyze the ORR profile, the correct overpotential should be calculated to compare the catalytic properties.

Secondary, the HER mechanism has relatively simple reaction path, and only binding energy on a material is needed to represent the HER profile. In the same manner with ORR, the proton source for HER reaction is depend on the solution condition. The water substitutes the proton source when the solution is alkaline condition, and thus, the proton dissociation energy barrier also should be calculated on the surface of catalytic materials. For the alkaline solution, the water dissociation is rate determine step for HER process, and the hydrogen binding energy becomes stronger when the water dissociation barrier is lower based on Bell-Evans-Polanyi principles. [20] For the binding energy

calculation, the Gibbs free energy should be calculated from proton ion as follows:

$$\Delta G_{H^*} = \Delta E_{H^*} + \Delta E_{ZPE} - T\Delta S \text{ , (2-8)}$$

$$\Delta E_{H^*} = E_{M\text{-}H} - [E_M + E_{H^+(aq)}] \text{, (2-9)}$$

where ΔE_{ZPE} is calculated 0.04eV and ΔS is approximated to $-\frac{1}{2}S^0_{H_2}$. From that condition, the eq.2-8 can be represented as follows:

$$\Delta G_{H^*} = \Delta E_{H^*} + 0.241eV \text{ . (2-10)}$$

To substitute the Pt catalyst, the absolute value of calculated hydrogen adsorption energy needs to evaluate less than 0.1 eV for “proper” HER catalyst because the Pt catalyst shows 0.1eV adsorption energy.

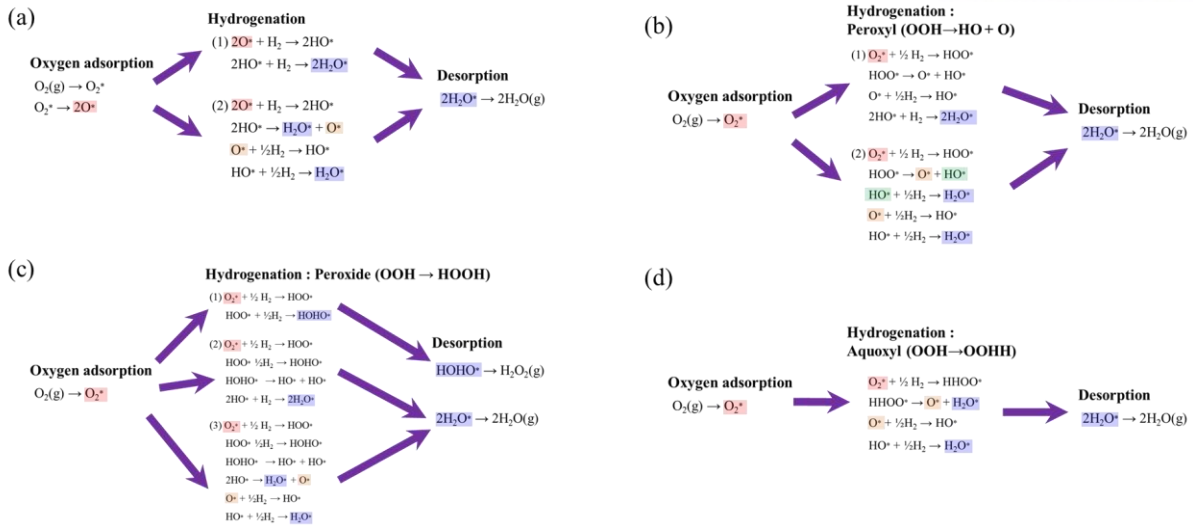

Figure 2-2. ORR paths: (a) hydrogenation, (b) hydrogenation for peroxyl, (c) hydrogenation for peroxide, and (d) hydrogenation for aquoxyle. Each color blocks guide for the oxygen atoms.

2.1.e. Group velocity in molecular dynamics

In the molecular dynamic (MD) simulation, the temperature is defined from the sum of kinetic energy of each “atom”. That calculated temperature has separation between simulated result and real situation. Even though each atom consisting on the molecule have high kinetic energy, the atoms are bound in the molecule. However, the total energy of a molecule is composed with translational, rotational, and vibrational energy. For that reason, the molecule temperature reflects real temperature and the translational and rotational kinetic energy affect the real temperature; the vibrational energy implies the latent heat of molecule. Classically, the translational energy and rotational energy are calculated as follows:

$$E_{trans} = \frac{1}{2}MV^2 = \frac{1}{2}M\left(\frac{1}{M}\sum m_i\vec{v}_i\right)^2, \text{ (2-11)}$$

$$E_{rot} = \frac{1}{2}I\omega^2 = \frac{1}{2}I\left(\frac{1}{I}\sum \vec{r}_i \times \vec{p}_i\right)^2, \text{ (2-12)}$$

, where m, v, r, and p indicate the mass, velocity, position, and momentum, respectively. Therefore, the molecular temperature can be defined by

$$\begin{aligned} T_{trans} &= 2E_{trans}/3 \\ T_{rot} &= 2E_{rot}/3 \end{aligned}, \text{ (2-13)}$$

$$T_{total} = T_{vib} + T_{trans} + T_{rot} = T_{latent} + T_{molecule}. \text{ (2-14)}$$

In the Figure 2-3, the computational temperature shows about 1000K although the molecular temperature indicates 200K. From that defined molecular temperature, the system is controlled by appling the thermostat to make constant temperature condition for MD.

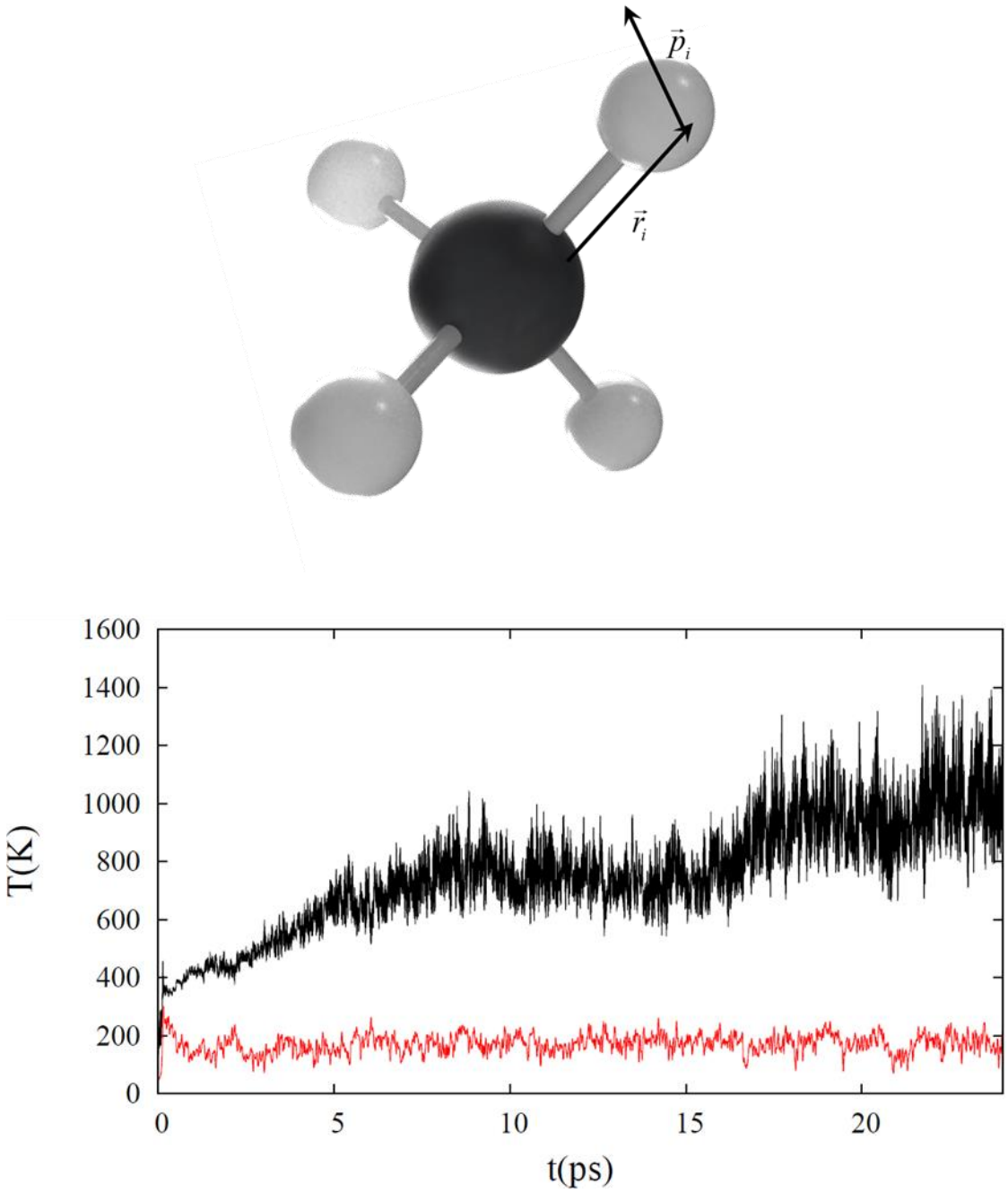

Figure 2-3. Group velocity simulation: Upper methane molecule guides for the symbol and Lower time-temperature graph represents the temperature variation; black and red solid line indicate the MD temperature and the group temperature, respectively.

2.2. Time dependent density functional theory

2.2.a. Introduction

The electron structure of ground state and the interconnected matter characteristics have been investigated by settling the Kohn-Sham equation. The electronic dynamics in the non-equilibrium state, however, cannot be represented by DFT simulation. In 1984, Erich Runge and Eberhard K. U. Gross reported a significant theorem for quantum time-dependent calculation. [21] That theorem demonstrated the one-to-one matching between time-dependent charge density and extrinsic potentials, and thus, it is interpreted the time-dependent edition for the Hohenberg-Kohn theorem. The time-dependent density functional theory (TDDFT) has been in progress based on the Hohenberg-Kohn theorem. [3, 22, 23] This theorem has been employed to research the optical features, light-matter coupling, and non-equilibrium dynamics in the materials. There are two different approaches in the TDDFT picture. One is the linear-response (LR) TDDFT, which calculates the optical features of a matter about the frequency realm such as the dielectric function. Another is the real-time propagation (RTP) TDDFT, which propagates the time-evolution of Kohn-Sham states by employing the time-evolution operator. In this thesis, the RTP-TDDFT is suggested to investigate the real-time non-equilibrium dynamics of charge density in the condensed matter.

2.2.b. Time-evolution operator in real-time propagation TDDFT

In the RTP-TDDFT picture, establishment of the time-evolution operator originated in the time-dependent Kohn-Sham equation is the initial step for time-propagation. The time-evolution operator is described as follows:

$$U\left(t+dt,t\right)=\exp\left(-i\frac{\hat{H}}{\hbar}dt\right) \quad (2\text{-}15)$$

The updated wavefunction at next time step is obtained by employing the time-evolution operator on the Kohn-Sham wavefunctions in the former time step as follows:

$$\psi\left(t+dt\right)=U\left(t+dt,t\right)\psi\left(t\right) \quad (2\text{-}16)$$

In the numerical calculation, there are diverse formula for time-evolution operator relying on the applied computational technique. For instance, the time-evolution operator splitting based on the Szuki-Trotter (ST) type has an exponential function. [4] The Kohn-Sham Hamiltonian consists with non-commuting kinetic, non-local, and local terms. To preserve the unitary properties of the non-commuting components of time-evolution operator, each part of exponential operators for the kinetic and non-local potential terms are divided by dimension of local potential term in the 2nd order time-evolution operators in ST type splitting as follows:

$$\begin{aligned}U_{2nd}^{ST}\left(t+dt,t\right)=&\exp\left(-i\frac{\hat{T}}{2\hbar}dt\right)\exp\left(-i\frac{\hat{V}_{NL}}{2\hbar}dt\right)\\&\times\exp\left(-i\frac{V_{Local}}{\hbar}dt\right)\exp\left(-i\frac{\hat{V}_{NL}}{2\hbar}dt\right)\exp\left(-i\frac{\hat{T}}{2\hbar}dt\right)\end{aligned} \quad (2\text{-}17)$$

Nevertheless, this ST type operator requires a high computational performance for applying the time-evolution operator in exponential function on the Kohn-Sham wavefunction. To avoid the high-cost required exact exponential form, the time-evolution operator of Crank-Nicholson (CN) type is employed as the solver of linear equation. As a result, it brings the more effective mathematical algorithm compared with the ST type time-evolution operator in the exact exponential function. The time-evolution operator picture in the CN type is founded on the time-reversal symmetric propagator between time-forward and time-backward wavefunctions as follows [22]:

$$U\left(t+\frac{dt}{2},t+dt\right)\psi\left(t+dt\right)=U\left(t+\frac{dt}{2},t\right)\psi\left(t\right) \quad (2\text{-}18)$$

By using the Taylor series for the exponential operator up to the first order, the time-evolution operator in the 2nd order CN type can be obtained as follows:

$$\psi\left(t+dt\right)=\frac{1-iHt/2\hbar}{1+iHt/2\hbar}\psi\left(t\right) \quad (2\text{-}19)$$

In the numerical simulation, Eq. 2-19 becomes more lucid linear equation problem when the Kohn-Sham Hamiltonian and wavefunction at a specific time, t, is given:

$$\left(1+iHt/2\hbar\right)\psi\left(t+dt\right)=\left(1-iHt/2\hbar\right)\psi\left(t\right) \quad (2\text{-}20)$$

To compare these two different time-evolution operators, ST and CN type, case studies in various system were performed. The numerical error of the total energy, $\delta E\left(t\right)=E_{tot}\left(t\right)-E_{tot}\left(0\right)$, is measured for the time-evolution of the stationary Kohn-Sham wavefunctions to make a comparison of the accuracy between the ST and CN type time-evolution operators, As an example, the time-propagation for the Al dimer system is evaluated by ST and CN type time-evolution operators with diverse time steps as depicted in Fig. 2-4(a). A smaller time step represents the more accurate time-propagation and shows the lowest numerical error in the Kohn-Sham total energy for the ST and CN type time-evolution operators. There is, however, an insignificant accuracy difference between the ST and CN type time-evolution operators. In Fig. 2-4(b), the computational performance is measured with diverse configurations: Al dimer, Benzene molecule, indolequinone-methide molecule, and so on. The cost for the calculation time of the ST type time-evolution operator is increased logarithmically with regard to the size of Kohn-Sham states. The computational performance for the CN type time-evolution operator is relatively decreased. For that reason, the time-evolution operator of the CN type is more useful for TDDFT simulation than that of the ST type.

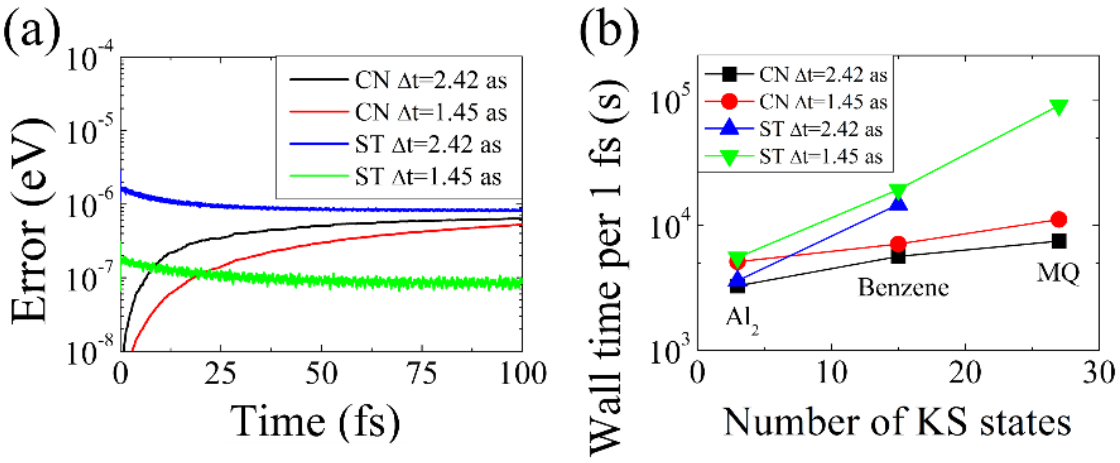

Figure 2-4. (a) Numerical error and (b) computation time cost for TDDFT calculation with various conditions.

2.2.c. Born-Oppenheimer and Ehrenfest dynamics

To estimate the condensed matter properties under the DFT picture, electronic and ionic structures are handled individually. The stationary electron is estimated by solving the Kohn-Sham equation. [24] The ionic dynamic is estimated by solving the Newtonian equation of motion with the Hellman-Feynman force term. In this scheme, the electronic systems are following the equilibrium state, or ground state, with the defined ionic location. This approach is founded on the Born-Oppenheimer approximation which postulates that there is a faster electronic dynamic enough to reach the ground state of electronic structure related with the ionic dynamic by a heavier atomic mass. The TDDFT simulation, however, can deal with the non-equilibrium electronic dynamics by employing the time-evolution operator. [22] As a result, the electronic and ionic dynamics can be depicted beyond the Born-Oppenheimer approximation. By computing the electronic and ionic dynamics with the same time step called Ehrenfest dynamics, the real-time dynamics of interaction between electronic and ionic structure can be estimated.

2.2.d. Vector potential in Ehrenfest dynamics

The Kohn-Sham Hamiltonian, wavefunction, and charge density are self-consistently solved through the time-dependent equation as follows:

$$i\hbar\frac{\partial}{\partial t}\psi_{n,\vec{k}}(\vec{r},t)=\left[\frac{1}{2m}(-i\hbar\vec{\nabla}+\frac{e}{c}\vec{A}_{ext})^2+\sum_{\lambda}v_{atom}(\vec{R}_{\lambda}(t))+V_{DFT}[\rho(\vec{r},t)]\right]\psi_{n,\vec{k}}(\vec{r},t)\text{ , (2-21)}$$

where n and k denote the band index and Bloch momentum vector, respectively. In eq.2-21, the external electric field is introduced and expressed using the velocity gauge of vector potential formula as follows:

$$\vec{E}(t)=-\frac{1}{c}\partial\vec{A}_{ext}(t)/\partial t\text{ . (2-22)}$$

To generate alternative current (AC) type electric field, the $\vec{A}_{ext}(t)$ sets sinusoidal form with a constant frequency. For dealing with it later, the multi-frequency wave is needed to generate to evoke effective resonance. For that reason, the $\vec{A}_{ext}(t)$ is modified to envelop-sinusoidal function.

III. Oxygen reduction reaction

3.1. Introduction

In the material science and catalyst field, the ORR has been raised for fuel cell and green energy generation. The process of generation of current through the ORR mechanism do not emit the greenhouse gases. However, the ORR catalyst has several serious problems such as durability, high cost, or CO poisoning. Currently, the Pt metal is one of a famous catalyst for ORR even though the cost is not cheap. The overpotential of Pt is about 0.78eV and it implies that the 0.78eV is needed to make the current flow. [25] However, the Pt catalyst has a CO poisoning problem, the carbon monoxide covering the catalytic surface, caused by two-electron process, and that problem is directly connected the durability of Pt catalyst. For these reasons, many researchers have investigated organic or cheap metal catalysts to substitute Pt metal. In this section, the core-shell structure metal catalyst and atomic doped graphene are introduced for ORR catalyst.

3.2. Carbon-Coated Core-Shell Fe-Cu nanoparticles as Highly Active and Durable Electrocatalysts for a Zn-Air Battery

To optimize the ORR process, the noble-metal-based catalysts such as Pt metal have been investigated extensively both theoretically and experimentally. However, the development of noble-metal-free allow catalyst is challenging with comparable catalytic activity and durability to noble-metal-based catalyst. From the volcano plots, the highest activity for oxygen reduction among the transition metal is Cu and the strong binding affinity with oxygen among the transition metal is Fe. Therefore, the alloy of Cu and Fe can substitute the previous Pt metal catalyst. The CuFe alloy nanoparticles can be synthesized experimentally, and the electrochemical test occurs in alkaline condition because of the corruption of Fe metal. For that reason, the CuFe alloy configurations are suggested for the location of Fe ions and the electrochemical profile is calculated by the DFT.

As the Figure 3-1 depicted, the combination of strong binding affinity and high activity metal can substitute the Pt metal catalyst. Therefore, the three-type configurations of CuFe alloy, Fe metal on the surface, Fe metal in the surface, and no Fe metal in the surface, are suggested. The Lower in Figure 2-1 describes the ORR processes on the CuFe alloy, and the Figure 2-2 represents the ORR profiles following the Figure 2-1 processes. The solution condition for the DFT simulation is alkaline condition, hydroxide rich and providing proton from water, because the acid condition dissolves the Fe metal from CuFe alloy. In the overpotential perspective, The $CuFe_{inner}$ shows the best profile, -0.6 eV, comparing to the $CuFe_{surface}$ alloy, -0.97V. A better ORR catalyst shows that the energy for each ORR step is decreased constantly. For the $CuFe_{surface}$ case, however, the oxygen binding is strong, and the energy drop in 0→1 step is high. This abrupt energy drop evokes the high overpotential to make downhill energy profile. The hydroxide binding energy on pure Cu metal is also high, and it disrupts the better energy profile. For these reasons, the $CuFe_{inner}$ shows the better performance, and the non-noble-metal-based can substitute the previous noble-metal-based catalyst such as Pt.

The lower energy profiles in Figure 2-2 indicate the energy profile of Cu, $CuFe_{inner}$, and $CuFe_{surface}$ in acid condition, respectively. The 0.4 eV is the equilibrium potential for ORR in alkaline solutions to make zero potential in 0 step. The net reaction of ORR has 1.6 eV potential for four-electron reaction, and the potential becomes zero when the applied potential is 0.4 eV (1.6 eV/4 electrons).

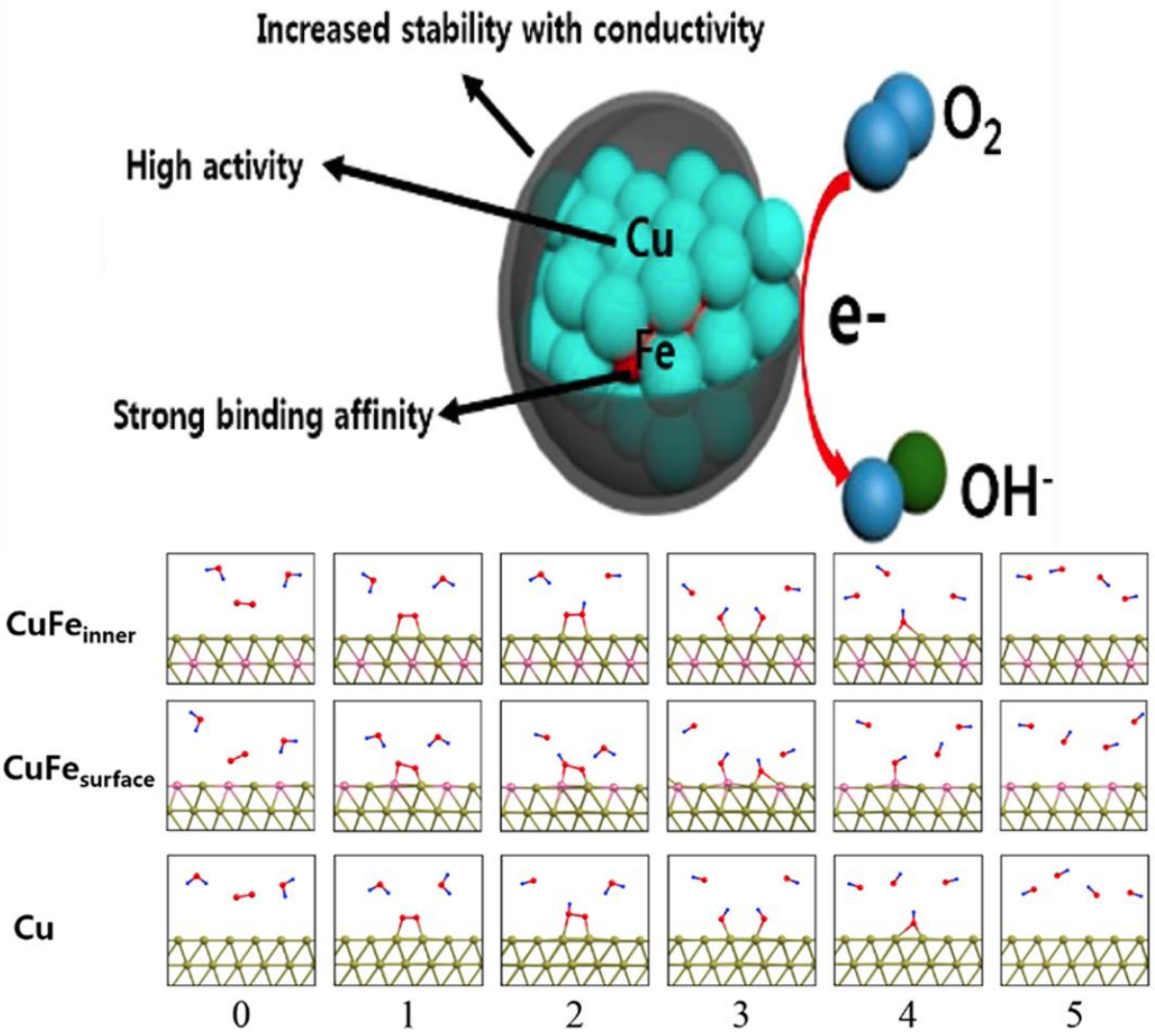

Figure 3-1. Upper represents a schematic configuration of electrochemical mechanism of CuFe alloy. Lower indicates the ORR processes for various locations of Fe metal.

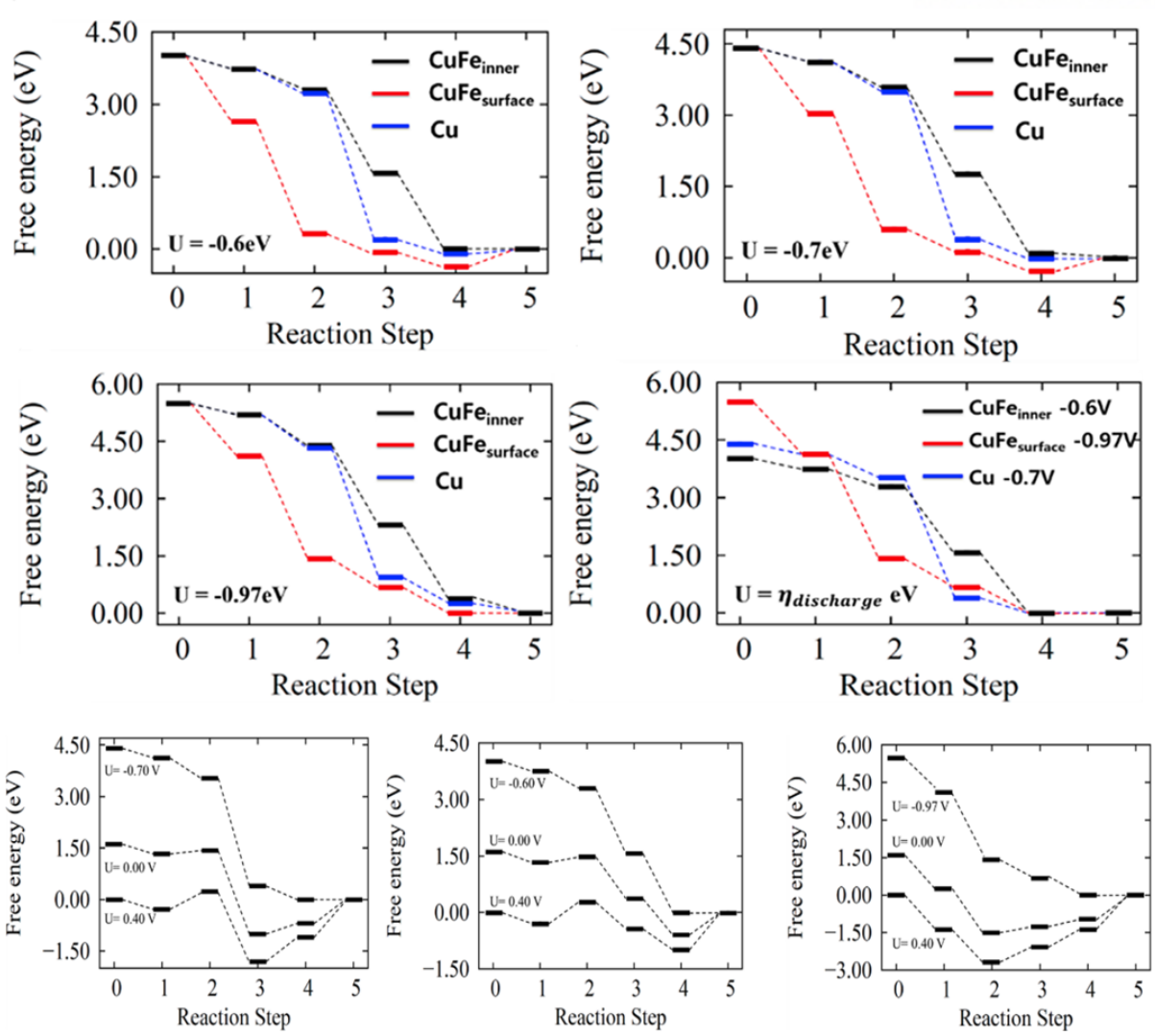

Figure 3-2. The electrochemical profile of CuFe alloy: various overpotentials for the ORR process.

3.3. Antimony-doped graphene nanoplates

The heteroatom doping into the graphitic frameworks also have been investigated for non-metal-based catalyst to substitute the noble-metal-based catalyst. Herein, the semimetal antimony (Sb) at the edges of graphene is suggested. The multiple oxidation states of Sb, Sb3+ and Sb5+, are responsible for the ORR stability. This atomic doped graphene works in alkaline condition, and thus, the doped Sb binds a hydroxide ion in the initial state of ORR. As depicted in Figure 3-3 and Figure 3-4, the Sb atom can be located both of armchair and zigzag edge sites. The oxygen dissociation process is rate determine step (RDF) for this ORR mechanism. The energy barrier in RDF for armchair configuration is lower than that for zigzag configuration, though the overpotential for armchair configuration is higher than that for zigzag configuration. To evaluate the stability, the association process is also compared to the dissociation process. The final state, H_2O_2 dissociation step, for the association process is endothermic reaction, and it implies the H_2O_2 poisoning cannot be happened. The various ORR pathways are scanned, and the ORR profiles for each pathway are calculated as Figure 3-5 shown. Among the various ORR pathways, the best process for armchair and zigzag edges are represented in Figure 3-4. For the zigzag edge case, all reaction step shows downhill. There is no reaction barrier if the oxygen dissociative adsorbed on Sb. For the armchair edge case, the 3→4 step shows small uphill even though the dissociation barrier is low.

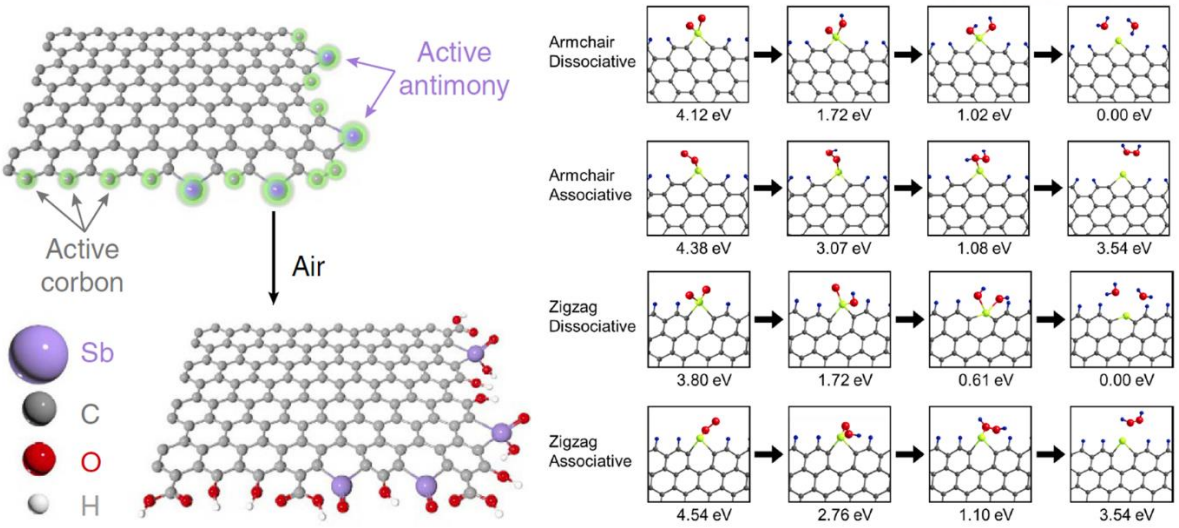

Figure 3-3. The schematic configuration of Sb doped graphene, and the energies for dissociation and association steps for armchair and zigzag type Sb doped graphene.

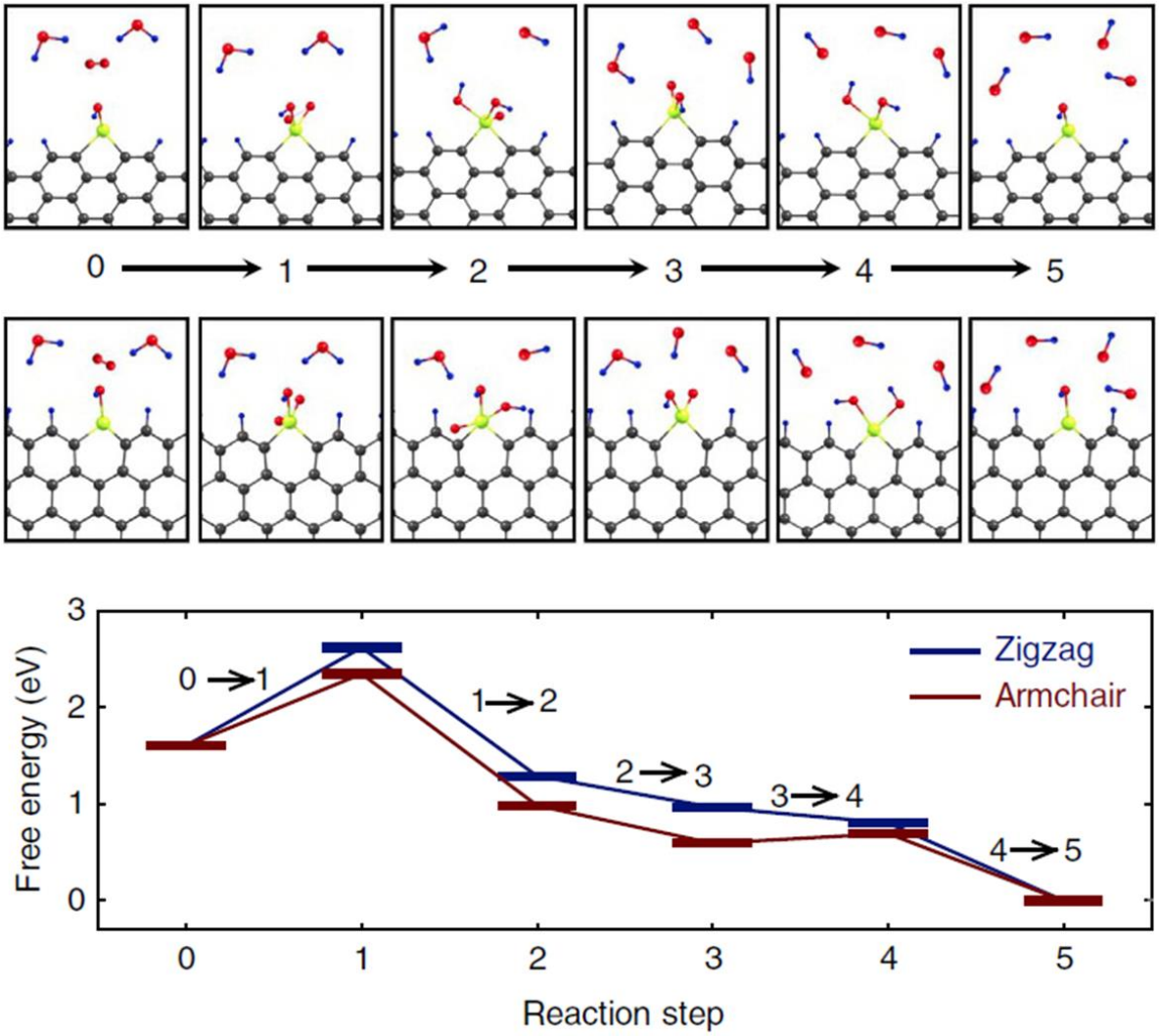

Figure 3-4. Free energy profile along the ORR reaction processes on the armchair and zigzag edges, and atomic configurations at each process.

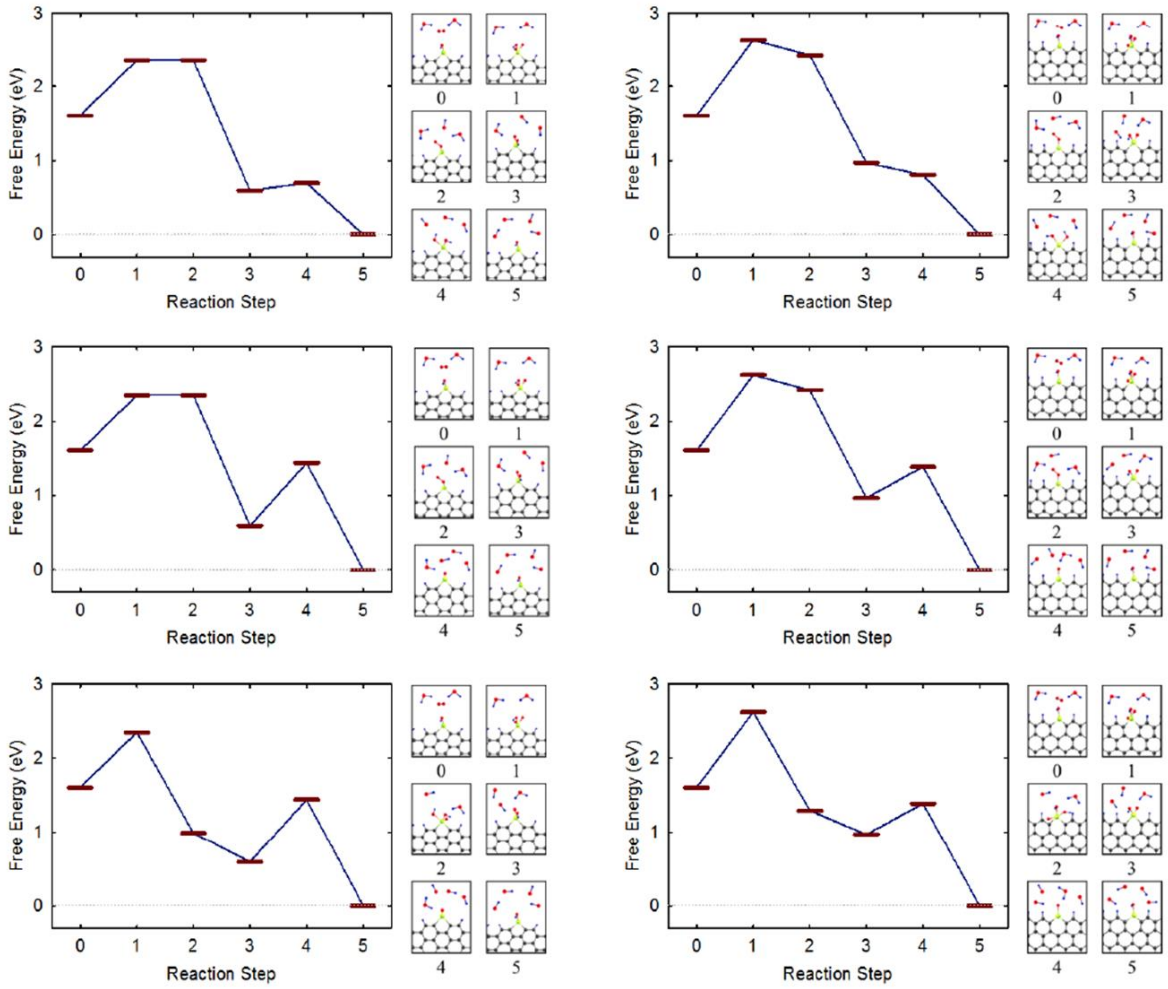

Figure 3-5. ORR energy profile along various reaction paths.

Reaction step	Reaction path
0→1	$Sb\text{-}OH + O_2 + 2H_2O + 4e^- \rightarrow Sb\text{-}OH(O_2) + 2H_2O + 4e^-$
1→2	$Sb\text{-}OH(O_2) + 2H_2O + 4e^- \rightarrow Sb\text{-}OH(OOH) + OH^- + H_2O + 3e^-$
2→3	$Sb\text{-}OH(OOH) + OH^- + H_2O + 3e^- \rightarrow Sb\text{-}OH(O) + 2OH^- + H_2O + 2e^-$
3→4	$Sb\text{-}OH(O) + 2OH^- + H_2O + 2e^- \rightarrow Sb\text{-}OH(OH) + 3OH^- + e^-$
4→5	$Sb\text{-}OH(OH) + 3OH^- + e^- \rightarrow Sb\text{-}OH + 4OH^-$

Table 3-1. Detailed reaction processes at each intermediate step.

3.4. Conclusion

The various reaction pathways need to be considered, scanned, and calculated to obtain exact overpotential and reaction path. To maximize the electrochemical catalyst performance, the free energy diagram should be constantly decreased. For that case, the equilibrium potential is 0.4 eV and overpotential is 0.4 eV, that is ideal ORR catalyst. The thermodynamical treatment and solution condition are also important. The phase of reactant and product should be considered. The poisoning problem, or hydroperoxide production, is needed to be checked. If the poisoning process is not forbidden, the stability of ORR catalyst is not enough to be utilized.

IV. Hydrogen evolution reaction

4.1. Introduction

In the material science and catalyst field, the HER has been investigated also for fuel cell and green energy generation. The HER process is simpler than ORR process, but the detailed thermodynamical treatment is needed to obtain more exact hydrogen binding energy. Otherwise the ORR process, the HER has only one pathway, but the criteria for application is strict. Currently, the Pt metal is also one of a famous catalyst for HER, and it has extremely weak hydrogen binding energy, less then 0.1eV. To substitute this Pt catalyst, the suggested catalyst should show the binding energy less than 0.1eV. In this section, the curved MoS_2 and 2D titanium carbide MXene are introduced for HER catalyst.

4.2. In situ Electrochemical Activation of Atomic Layer Deposition coated MoS2 Basal Planes for Efficient Hydrogen Evolution Reaction

The Molybdenum disulfide, MoS_2, composing of active edge sites and a catalytical inert basal plane is a raising catalyst to substitute the noble-metal-based catalyst such as Pt for electrochemically catalyzing HER. Because the MoS_2 is 2D material and the basal plane consists of the majority of MoS_2 layer, the activation of basal plane is an important challenge to enhance the HER performance. Herein, the MoS_2 basal plane is activated when the basal plane is distorted such as convex or concave distortion. As depicted in Figure 4-1, there are some convex planes when TiO_2 is dissolved, and various angles of convex are investigated. Even though the absolute value of binding energy is not satisfied to proper HER catalyst, the binding energy enhancement is noticeable. The non-treated MoS_2 basal plane has very high binding energy, about 2.3 eV, but the convex MoS_2 basal plane shows less than 1.0 eV. The binding weakness follows the trend of charge states of S and Mo atoms. When the convex angle is larger, the charge transfer from Mo to S is higher. The charge transfer makes surface more negative charge. The negative charge surface drags the positive charge proton, and the HER performance is enhanced. This research shows that relationship between surface charge state and hydrogen binding energy clearly.

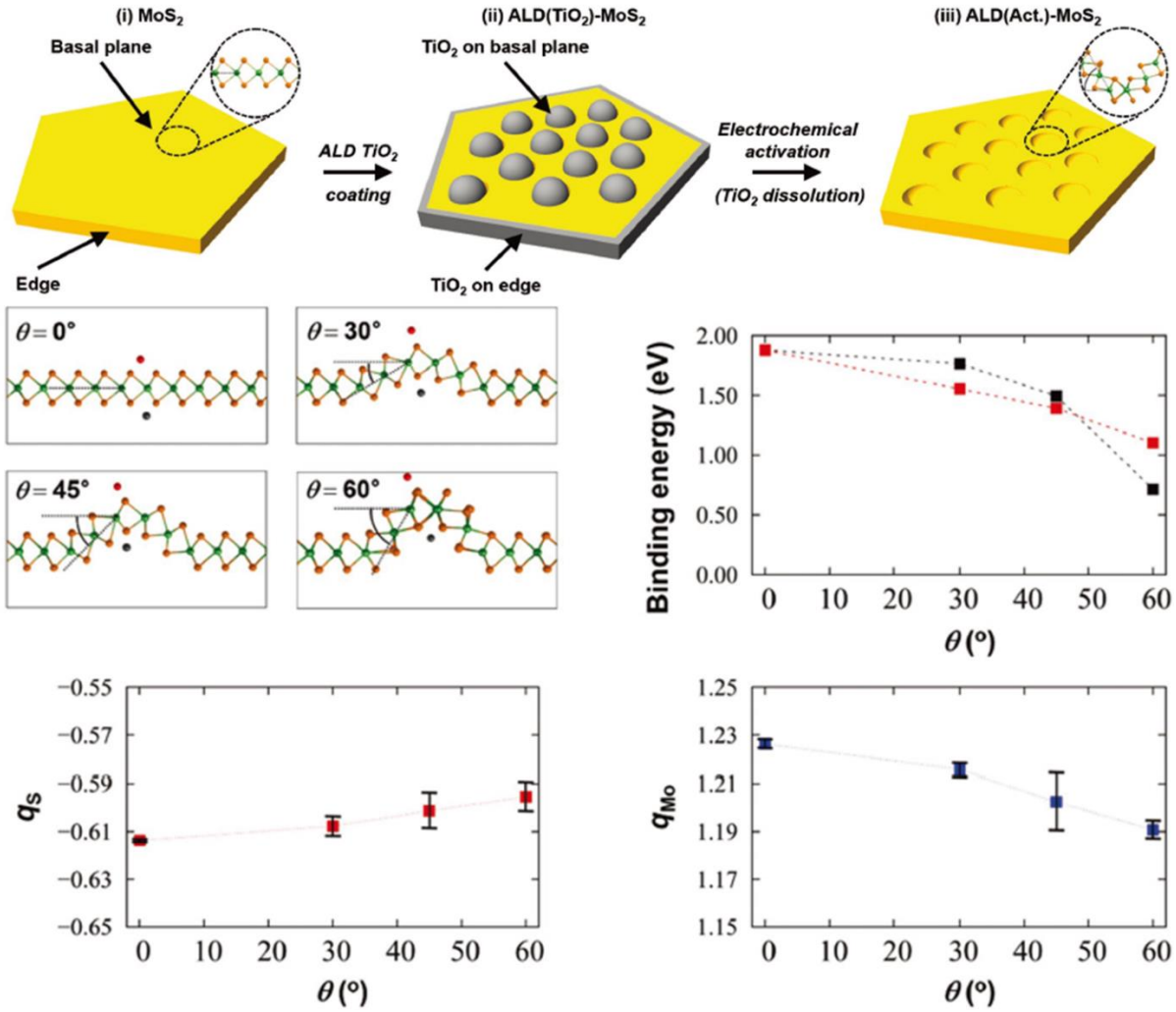

Figure 4-1. The configurations of convex MoS2 basal plane. Binding energy and charge states of molybdenum and sulfur atom on convex surface.

4.3. Enhanced Electrocatalytic Activity by Chemical Nitridation of 2D Titanium Carbide MXene for Hydrogen Evolution

Developing active and stable electrocatalysts is the goal for water splitting for HER. The titanium carbide MXene is one of a promising material to substitute the previous Pt catalyst. As Figure 4-2 depicted, The MXene is stacked layer structure, and each layer is binding with the Al atoms. Therefore, the substitutional sites at surface should exist, and various compound or atom adsorbs at there. Following the experimental condition, six types, simple vacancy, oxygen, nitrogen, aluminum, fluorine, and hydroxide, can occupy the substitutional sites. The simulated results indicate the nitrogen substitution is the only possible candidate for HER process. For vacancy and aluminum treated surface case, the Gibbs free energy for hydrogen binding is highly positive, 2.61 eV and 3.99 eV, respectively. In the case of fluorine substitution, the Gibbs energy is within proper range, 0.15 eV, but the hydrogen atom is not adsorbed on fluorine atom, and instead detached the other hydrogen atoms on the hydroxyl site and formed a hydrogen molecule. For that reason, fluorine substituted surface is not proper for hydrogen adsorption. On the other hand, the nitrogen treated surface is not only has low formation energy, 0.97 eV, but also low Gibbs free energy, -0.34 eV. That results imply that nitrogen substitution on the surface of MXene shows effective way of making an efficient electrocatalyst for HER process.

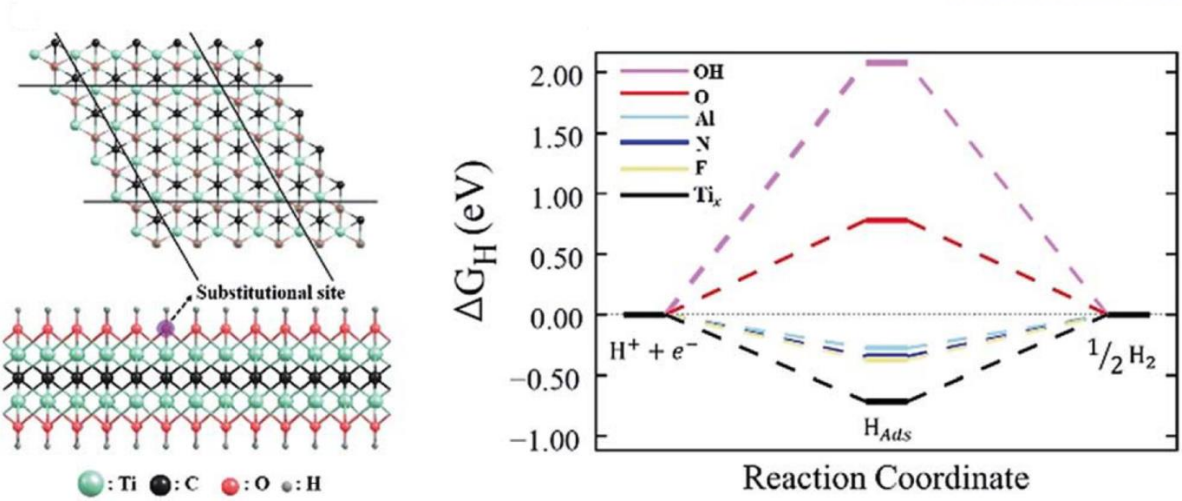

Figure 4-2. The configuration of titanium carbide MXene structure and Gibbs free energies for hydrogen binding at various reaction sites.

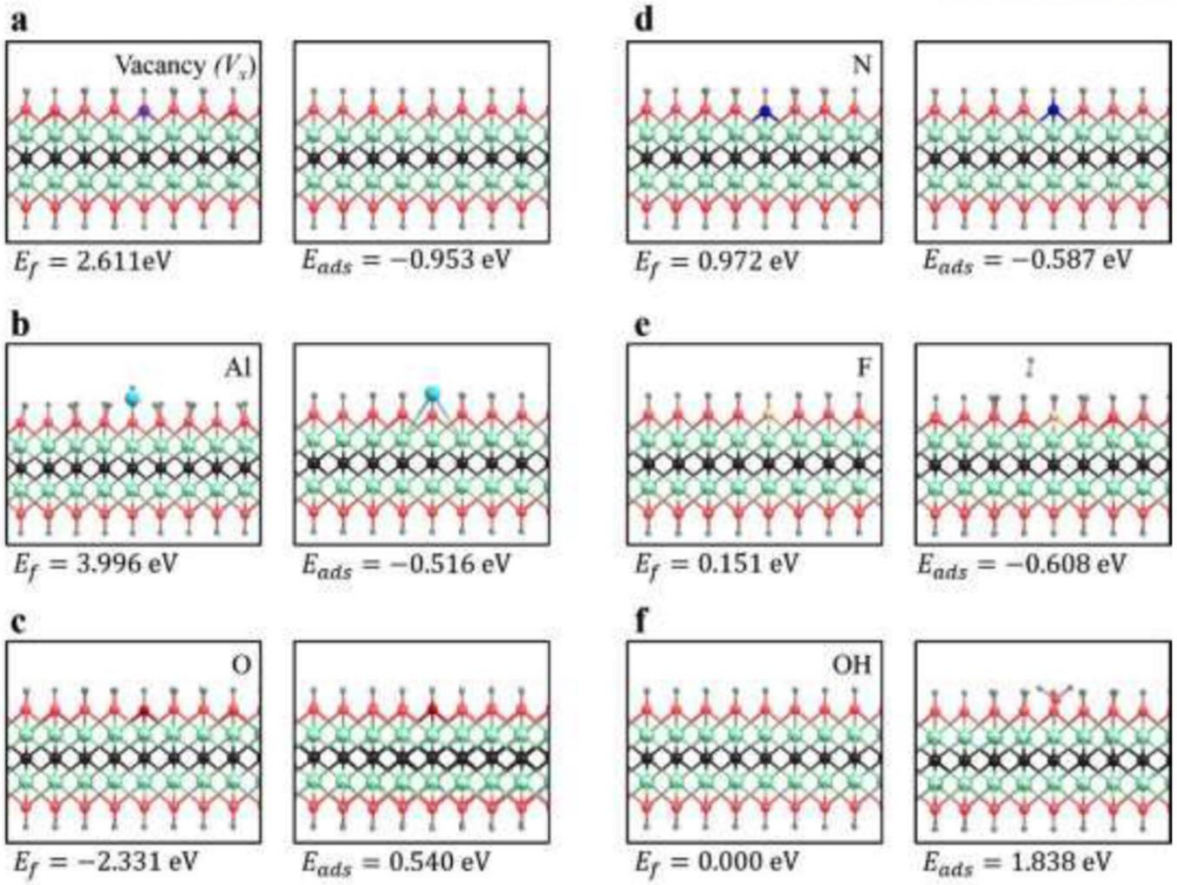

Figure 4-3. The configurations for doped and defected MXene structure with vacancy, aluminum, oxygen, nitrogen, fluorine, and hydroxide, respectively.

4.4. Conclusion

For the high performance HER catalyst, the thermodynamically treated Gibbs free energy for hydrogen binding is ranged in 0.1eV to substitute the Pt catalyst. To enhance the HER performance, the catalyst surface should have negative charge to drag the proton ions to the surface. The high binding energy, however, makes hard to detach the generated hydrogen molecules from the surface. The balance between binding affinity and detachment should walk a fine line. To satisfy that condition, two types for non-metal-based and non-noble-metal catalyst are suggested, convex MoS_2 and MXene. The fundamental concept to enhance the HER performance is same, that is making a negatively charged surface. Both of treatments make successively the Gibbs free energy for HER ranged in proper region.

V. Anharmonicity in molecular vibration

5.1. Introduction

Manipulations of materials by using strong laser pulses have attracted various scope of interest for quite long time. For solid states, the optical controls have mainly targeted at collectively ordered states, such as magnetism and ferroelectricity, or even electro-optical response functions. [26-30] On the other hands, for molecules, the lighting has aimed at transferring energy to promote desired chemical reactions. Since bond dissociation is an essential prerequisite for most of chemical reactions, an effective bond cleavage has been the most central issues in the design catalyst or any related chemical reactions. Among noticeable examples in this perspective, Hundt et al, applied infrared field, in resonance with the O-H stretching vibration, to promote the water dissociation on Ni(111) surface,[31] Jiang et al. studied another candidate, carbon dioxide, on Ni(100) surface with excitation of CO2 bending mode.[32]

Activation of chemical bonds to the regime of bond cleavage is distinctly different from the vibration activation near harmonic range. For example, when a bond approaches the cleavage regime, the potential energy surface (PES) deviates from the harmonic quadratic form, and the anharmonic should obviously involves multiple frequency components. A delicate combination of various frequency lights may result in a tunable excitation of selected chemical bonds. In this perspective, Levis et al. have investigated the effect of the few-frequency laser pulses, determined from randomly generated components of pulse through a genetic algorithm; the combination of different frequency waves was shown to have an apparent effect,[33] but the relation between the selected light frequencies and characteristic energy scales of materials has not been discussed to date.

5.2. Potential energy surface

When a molecule is vibrating, the motions of each component follows the potential energy surface (PES) of each vibration mode. There are two modes, stretch and bending mode, between two near atoms consisting of a molecule. The PES of stretch mode commonly follows the morse potential formula, and that of bending mode is simple quadratic function. In this thesis, the target molecules are methane for example of stretch mode and carbon dioxide for example of bending mode. As Figure 5-1(a) depicted, the PES of C-H stretch mode shows the morse potential function as follow:

$$V(X) = D_e[e^{-2(X-X_e)a} - 2e^{-(X-X_e)a}] \quad (5\text{-}1)$$

, where D_e, X_e, and a are 6.53303 eV, 1.12319Å, and 1.61181Å^{-1}, respectively. For the carbon dioxide case, the PES of O-C-O bending mode is simple quadratic function as follow:

$$V(\theta) = \varepsilon\theta^2 \quad (5\text{-}2)$$

, where ε is 7.0543·10^{-4} eV/degree^2 from Figure 5-1(c).

For the short-range vibration, the stretch mode is able to be assumed to a simple quadratic function, or simple harmonic oscillation. However, the harmonicity is broken when the stretch mode is amplified, and that simple harmonic oscillator becomes an anharmonic oscillator. The harmonicity and anharmonicity will be discussed later.

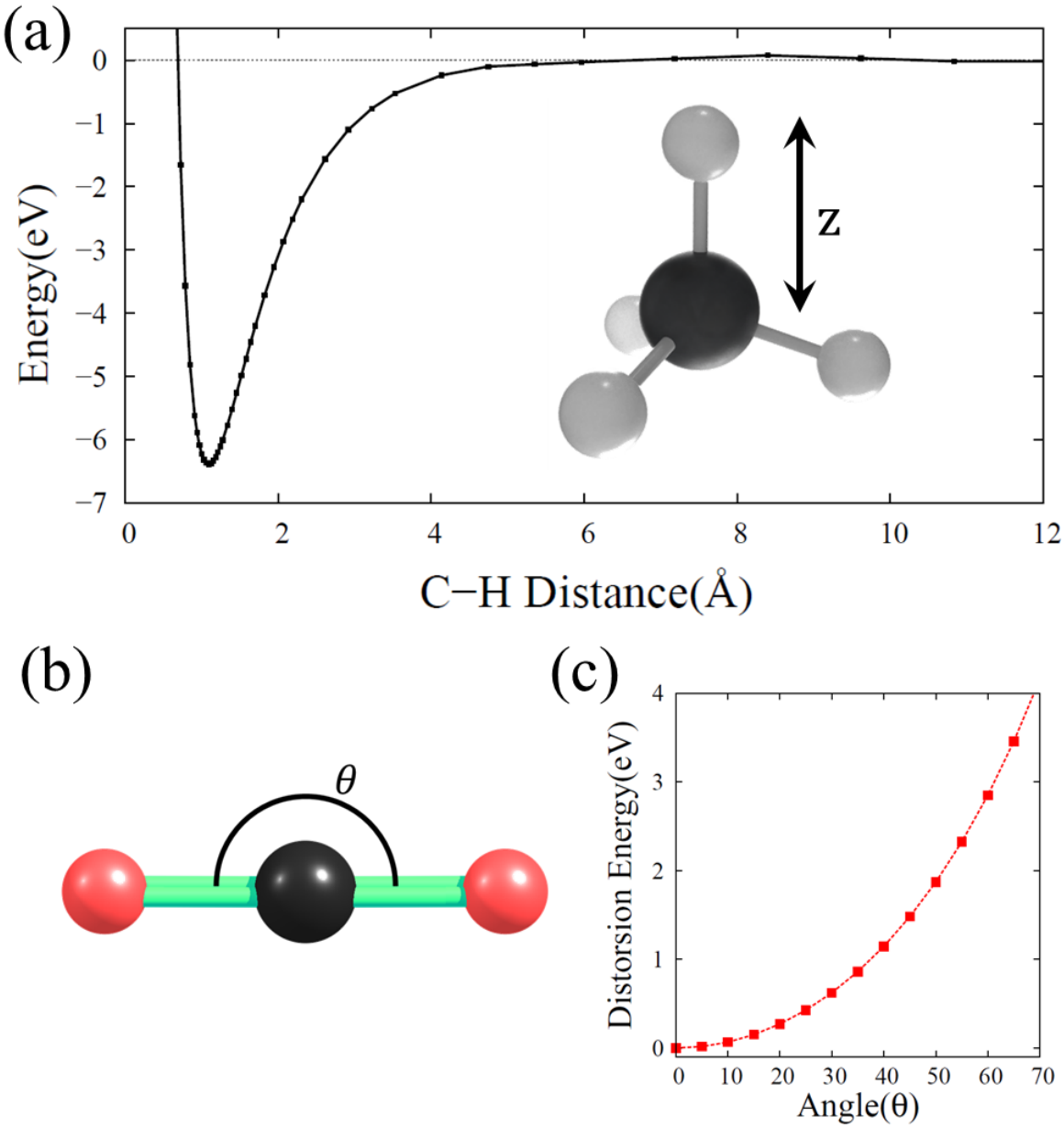

Figure 5-1. (a) The potential energy surface for C-H stretch mode along the z-direction. (b) The molecular configuration of carbon dioxide and (c) the potential energy surface for the carbon dioxide bending mode. θ symbol indicates the O-C-O angle.

5.3. Classical model

The molecular vibration and resonance can be interpreted by the equation of motion. In the equation of motion of driven harmonic oscillator, the Newton's second law takes the form

$$F(t) - kx - c\frac{dx}{dt} = m\frac{d^2x}{dt^2}. \quad (5\text{-}3)$$

When the driving force is alternative current field, the $F(t)$ is $E_0 e^{i\omega t}$, where E_0 and ω are amplitude and frequency of the field. However, in the molecular stretch mode, the oscillator is not harmonic but anharmonic morse potential. To apply this anharmonicity, the equation 5-3 is changed to

$$m\frac{d^2X(t)}{dt^2} + \frac{dV(X(t))}{dx} = E_h e^{i\omega_h t} \quad (5\text{-}4)$$

, where $V(X(t))$ is the morse potential as represented in equation 5-1.

To solve the second order non-linear differential equation (equation 5-4), the finite difference coefficient is adopted, and the Figure 5-2 shows the effect of resonance. The harmonic frequency, ω_h, is calculated by $[E_1 - E_0]/\hbar$ from the energy level of morse potential. As Figure 5-2 depicted, the frequency of external field influenced the amplification of displacement. The 10% differences of frequency affect the displacement more than 50%. From this classical model, the envelope of wave occurs. This envelope implies that multi-frequencies exist for the molecular stretch mode, and it is the reason of anharmonicity of potential energy surface. Wang have investigated this envelope from the atomic trajectory for a sufficiently long molecular dynamics simulation at a low temperature. [34] From his research, the multi-order derivative approach is universal for the calculations of vibrational frequencies, and he calculated the anharmonic fundamental vibrational frequencies of several molecules.

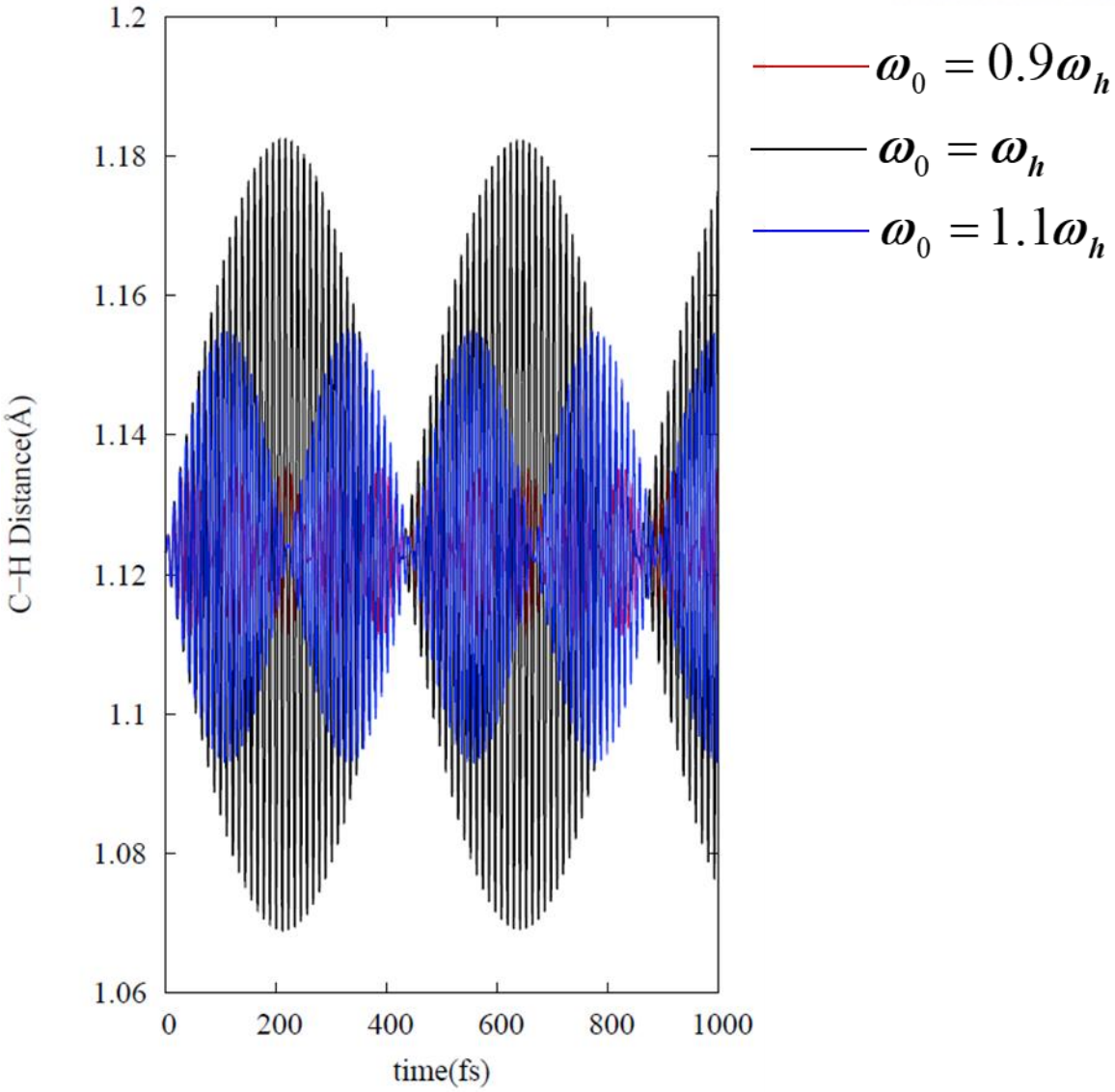

Figure 5-2. The displacements of C-H bond when external field is applied. The red, black, and blue line indicate the frequencies of applied field where $0.9\,\omega_h$, ω_h, and $1.1\,\omega_h$.

5.4. Harmonic and anharmonic frequency

From the potential energy surface and classical model, the anharmonic frequency is important factor beyond the harmonic oscillation. Morichika et al. have investigated that the combination of ultrafast optics and nano-plasmonic in the mid-IR range is useful for mode-selective vibrational ladder climbing. [35] They successively dissociated the carbonyl stretch vibration of W(CO)6 in n-hexane solution using both down-chirping and substantial field enhancement. The vibration modes were excited step-by-step along the frequencies, and this ladder climbing made to the resulting CO dissociation from W(CO)6.

For the carbon dioxide case, the potential energy surface for bending mode in Figure 5-1 (c) indicates that there is only harmonic frequency for resonance. As Figure 5-3 (a) depicted, the bending angle is about 5 degrees at the room temperature (300K) without external field, and it indicates about 0.01 eV is accumulated in the carbon dioxide bending mode according to the Figure 5-1 (c). When the external field with bending mode frequency is applied, the scissoring of carbon dioxide is intensified. In Figure 5-3 (b), the carbon dioxide bending mode is amplified to 15 degrees, and it indicates about 0.2 eV is accumulated in the carbon dioxide bending mode. From this result, it is confirmed that the real-time TDDFT with external vector potential can represent the resonance phenomena.

For the methane simulation, the harmonic frequency is scanned from 85 THz to 100 THz. Then the external field frequency is the 91.875 THz, the displacement of C-H bond is maximized as Figure 5-4 described. As Figure 5-5 depicted, the responses to external field are similar with the carbon dioxide case. The C-H stretch mode is not activated when the DC field and CO2 bending frequency field are applied. On the other hand, the C-H stretching is amplified when the C-H resonant frequency field is applied. When the C-H trajectory with resonant external field is plotted for long-time range, the envelope wave is appeared as Figure 5-6 (a) depicted. The envelope wave is multi-frequencies wave, and the Fourier transform of the envelope wave shows the components of frequencies. As Figure 5-6 (b) represented, there are two frequencies, one is harmonic frequency (91.876 THz) and another is anharmonic frequency (88.871 THz). When the two-frequency field, $\boldsymbol{E} = \boldsymbol{E}_h \boldsymbol{e}^{i\omega_h t} + \boldsymbol{E}_{ah} \boldsymbol{e}^{i\omega_{ah} t}$ where $\boldsymbol{E}_h$, ω_h, $\boldsymbol{E}_{ah}$ and ω_{ah} indicate the amplitude of harmonic field, harmonic frequency, amplitude of anharmonic field, and anharmonic frequency, respectively, is applied, the C-H stretch mode is evidently amplified as Figure 5-6 (c) depicted.

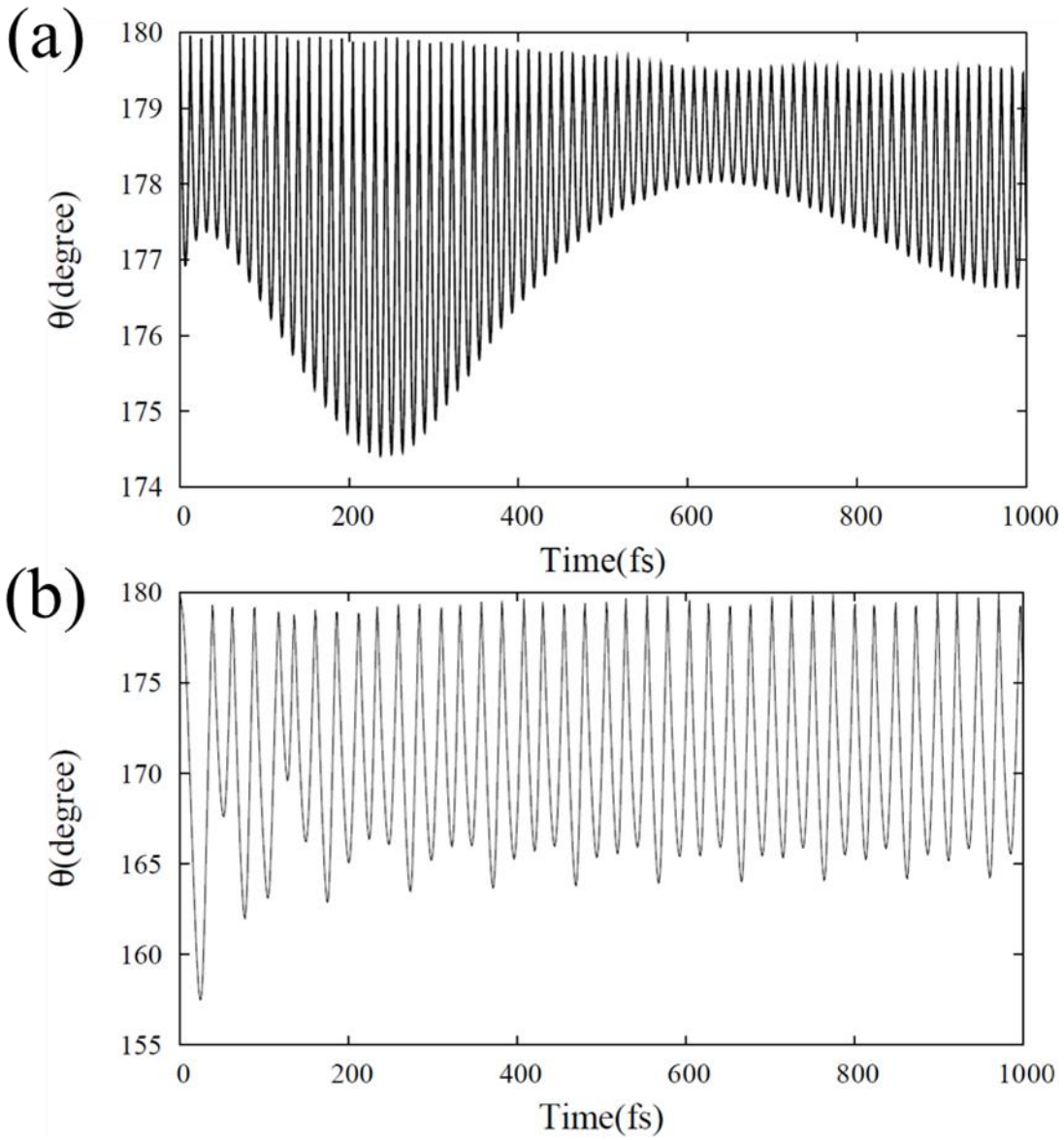

Figure 5-3. The O-C-O degree trajectory in carbon dioxide in Figure 5-1 (b) for (a) room temperature and (b) with external field with CO2 bending frequency (20.008 THz).

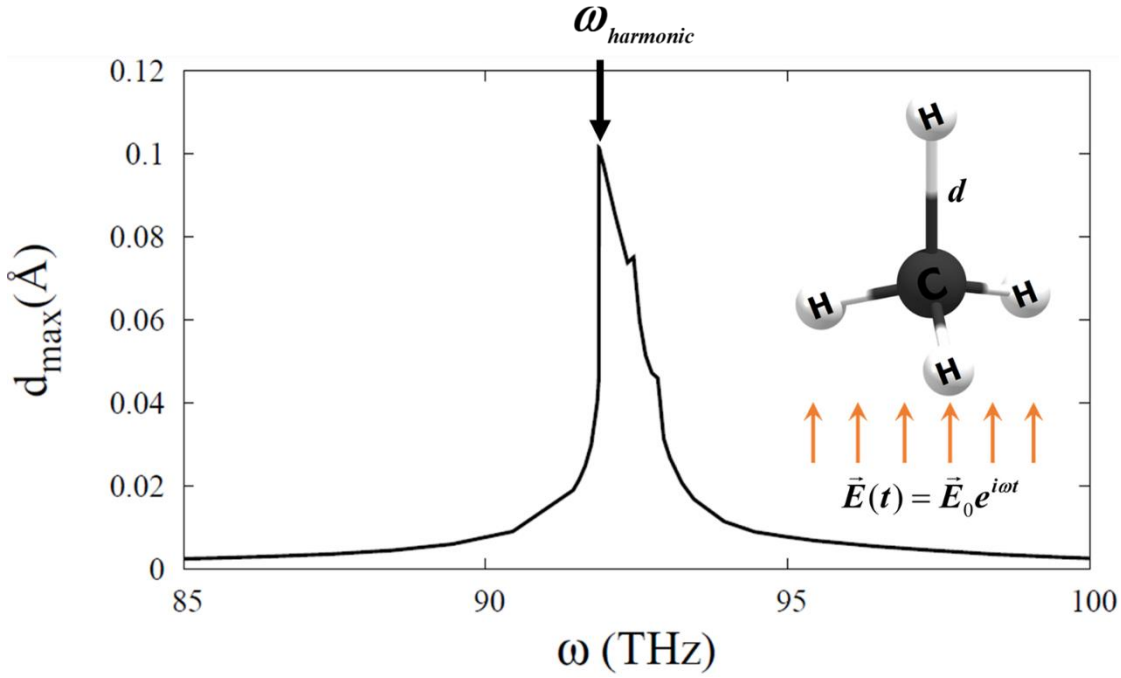

Figure 5-4. The frequency scanning for a methane molecule. $\boldsymbol{d}_{\max}$ and $\boldsymbol{\omega}_{harmonic}$ indicate the maximum of C-H displacement and frequency when $\boldsymbol{d}_{\max}$ shows the highest value, respectively.

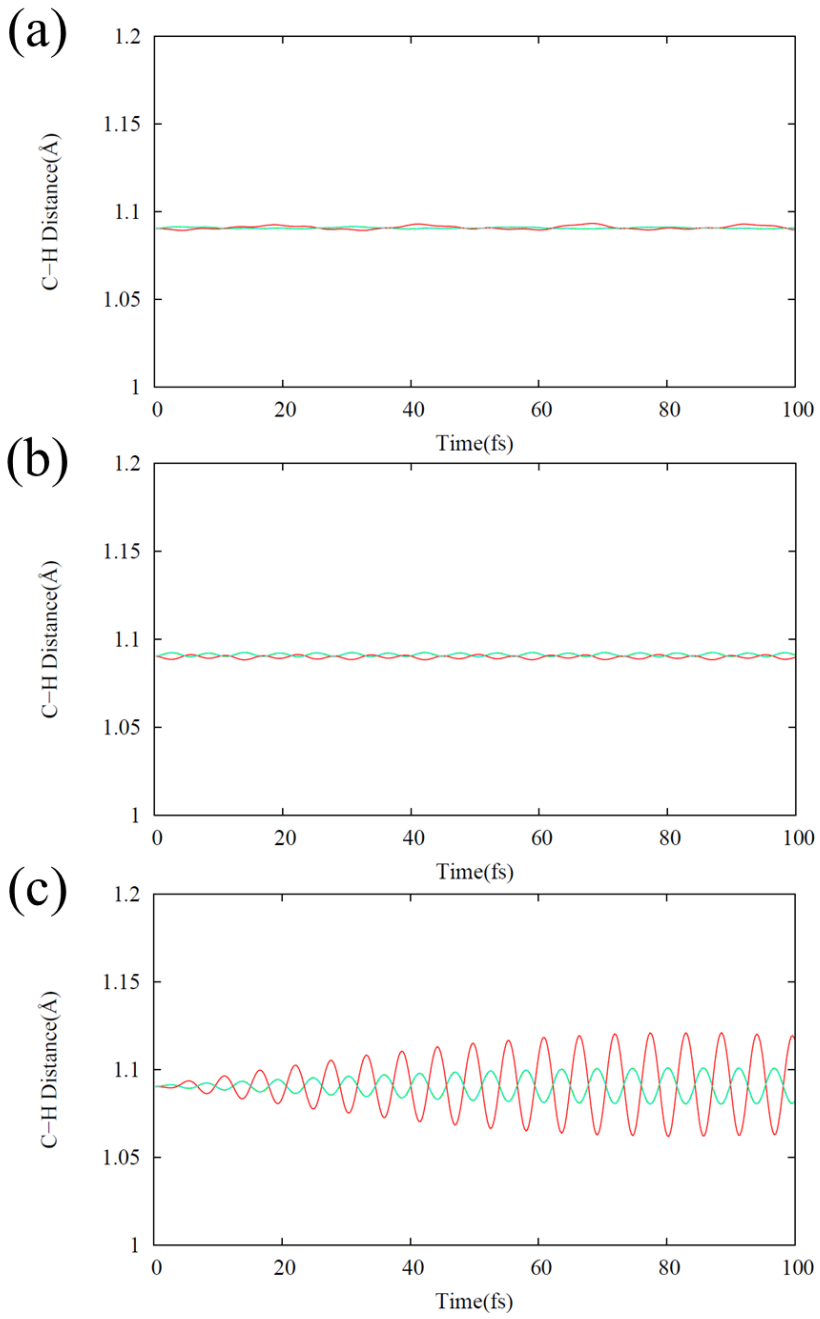

Figure 5-5. C-H vibrational trajectory in methane for various frequencies; (a) DC field (0 THz), (b) CO2 bending frequency (20.008 THz), and (c) CH4 stretch frequency (91.875 THz).

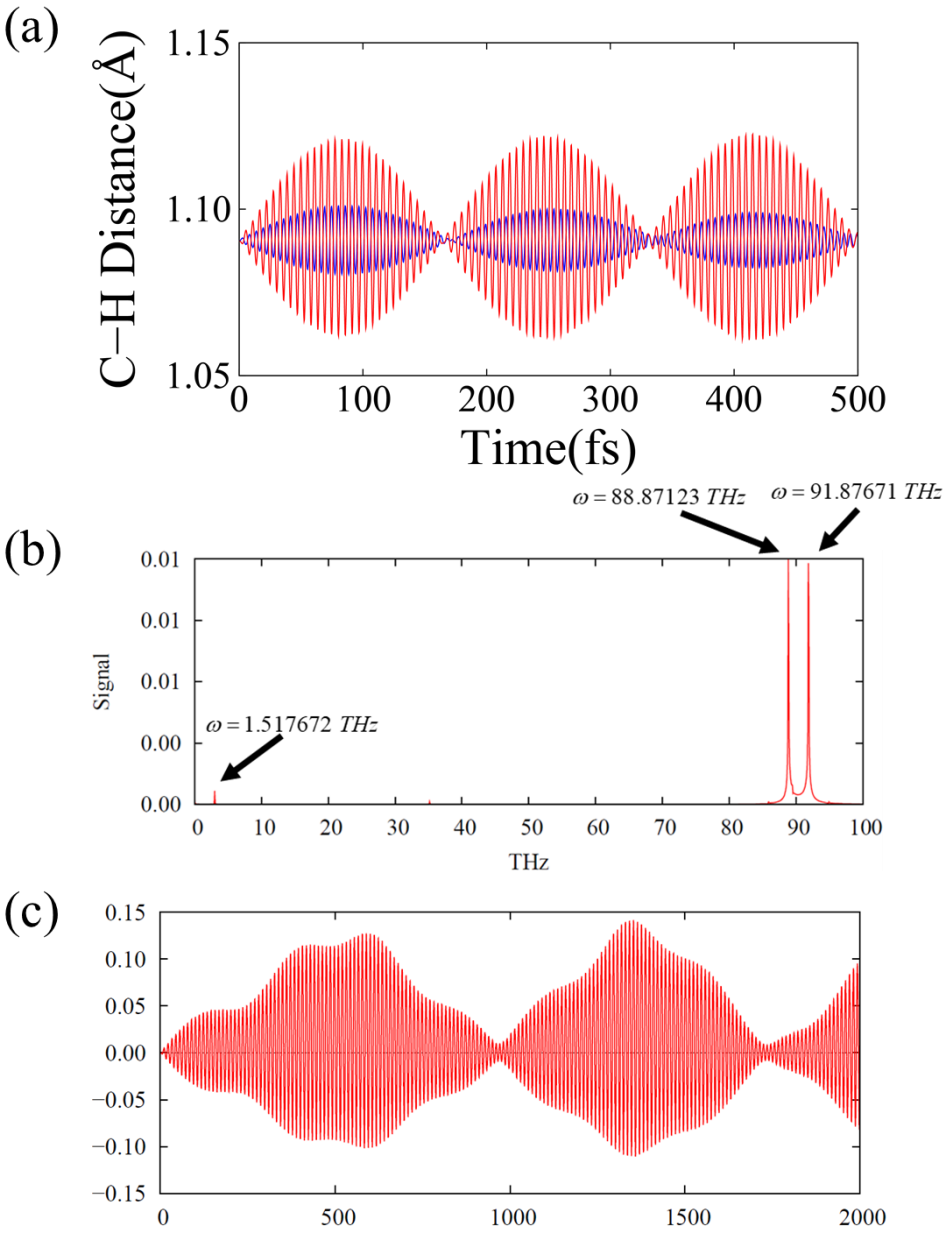

Figure 5-6. (a) The C-H trajectory for long time scale molecular dynamics simulation with single harmonic frequency field, and (b) the Fourier transform of a function of C-H trajectory. (c) The C-H trajectory with two-frequencies from Fourier transform data.

5.5. Amplitude effect

To analyze the effect of anharmonic frequency light, the maximum displacements with the pulse with single-frequency and two-frequency are compared according to the amplitude of light pulse. Basically, the maximum displacement is increased linearly depending on the amplitude of laser pulse. The effect of anharmonic frequency amplified the displacement remarkably. The combination of harmonic and anharmonic light is following the equation, $\boldsymbol{E} = \boldsymbol{E}_0 \boldsymbol{e}^{i\omega_{harmonic} t} + \boldsymbol{E}_0 \boldsymbol{e}^{i\omega_{anharmonic} t}$, that is, the amplitudes of harmonic part and anharmonic part are same. As Figure 5-7 depicted, at the weak amplitude less than 0.2 V/Å, the maximum displacement for combination of harmonic and anharmonic light, $\Delta \boldsymbol{d}_{\max}^{comb}$, is about five times greater than that for single harmonic light, $\Delta \boldsymbol{d}_{\max}^{harmonic}$. Furthermore, the $\Delta \boldsymbol{d}_{\max}^{comb}$ at the 0.2 V/Å is similar with the $\Delta \boldsymbol{d}_{\max}^{harmonic}$ at the 1.0 V/Å. From this result, the anharmonicity is the important factor to activate a molecule without high temperature with only light. In the real situation, the maximum amplitude of light is limited to 10 MV/cm, or 0.1 V/Å, and it is weak field region.

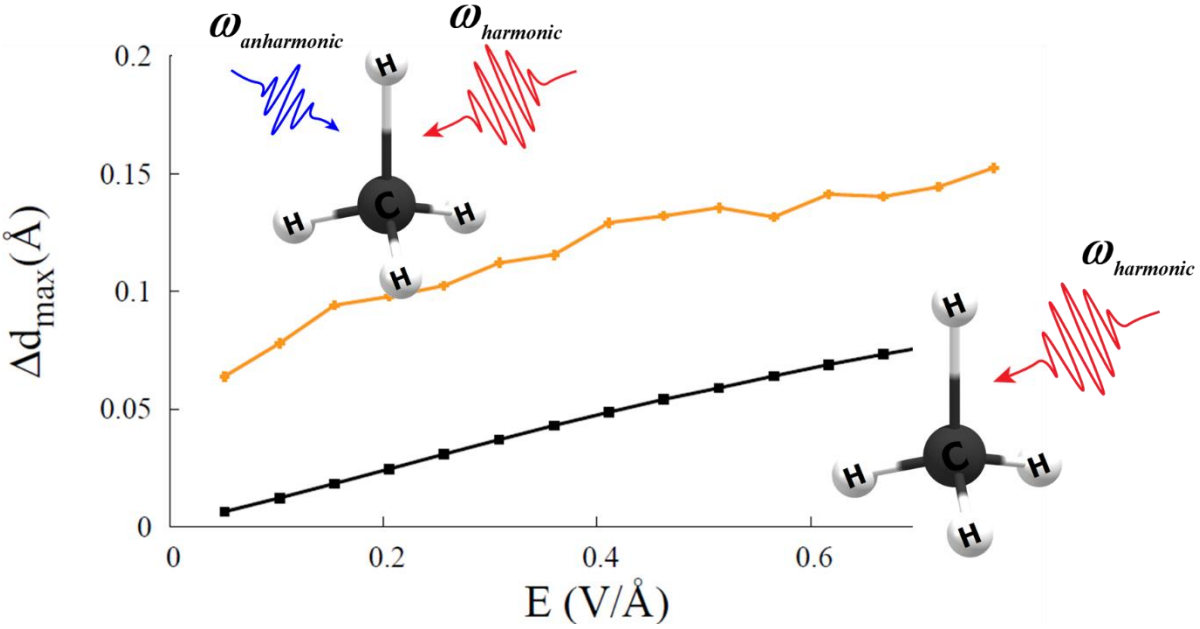

Figure 5-7. The maximum displacements according to the amplitude of laser pulse; black and orange line indicate the maximum displacements for the pulse with the single harmonic frequency and the combination of harmonic and anharmonic frequencies, respectively.

5.6. Molecular dynamics

For the carbon dioxide case, there is only harmonic frequency can influence on the reaction. The rate determine step for carbon dioxide capturing or transforming is adsorption of carbon dioxide on catalytic surface step. [36] Commonly, the carbon dioxide is non-polar gas and hard to activate on a catalytic surface, and the energy barrier between physisorption and chemisorption state is main obstacle for carbon dioxide adsorption. In the Figure 5-8, the carbon dioxide goes away from the Cu (110) surface without any external light pulse. The carbon dioxide, however, is dragged to the Cu (110) surface when the external light pulse with O-C-O bending frequency is applied, and it overcomes the barrier between physisorption and chemisorption state. From the molecular dynamics simulation results, the first rate determine step for carbon dioxide capturing can be overcame easily by using external light pulse.

For methane case, the methane is one of hydrogen carrier molecule, and the hydrogen gas can be produced from methane gas. As Figure 5-9 (a) described, the supercell is consisting on 8 methane molecules with liquid methane density. In this situation, the methane molecules are transformed to hydrogen molecules and carbohydrate molecules as follows:

$$\begin{aligned} 2\boldsymbol{CH}_4 &\rightarrow \boldsymbol{H}_2(\boldsymbol{g}) + \boldsymbol{C}_2\boldsymbol{H}_6 \\ 2\boldsymbol{CH}_4 &\rightarrow 2\boldsymbol{H}_2(\boldsymbol{g}) + \boldsymbol{C}_2\boldsymbol{H}_4 \\ 2\boldsymbol{CH}_4 &\rightarrow 3\boldsymbol{H}_2(\boldsymbol{g}) + \boldsymbol{C}_2\boldsymbol{H}_2 \\ 2\boldsymbol{CH}_4 &\rightarrow 4\boldsymbol{H}_2(\boldsymbol{g}) + \boldsymbol{C}_2(\boldsymbol{s}) \end{aligned} \quad . \text{(5-5)}$$

From the result in this part, the effect of light pulse with the combination of harmonic and anharmonic frequency is confirmed. The Ehrenfest dynamics simulation with that laser pulse represents that the distribution of inter-bonging of H-H is increased and distribution of C-H bonding is decreased as time goes on as Figure 5-9 (b) depicted. It indicates that the hydrogen atom in methane is dissociated, it reacts with other detached hydrogen atom, and the new hydrogen molecule is generated. In the real industry, the hydrogen formation from methane requires high temperature and high pressure. It requires high energy costs and expensive production facilities. However, this novel mechanism is suggested to substitute that previous process with low energy cost, or just light pulse with frequency.

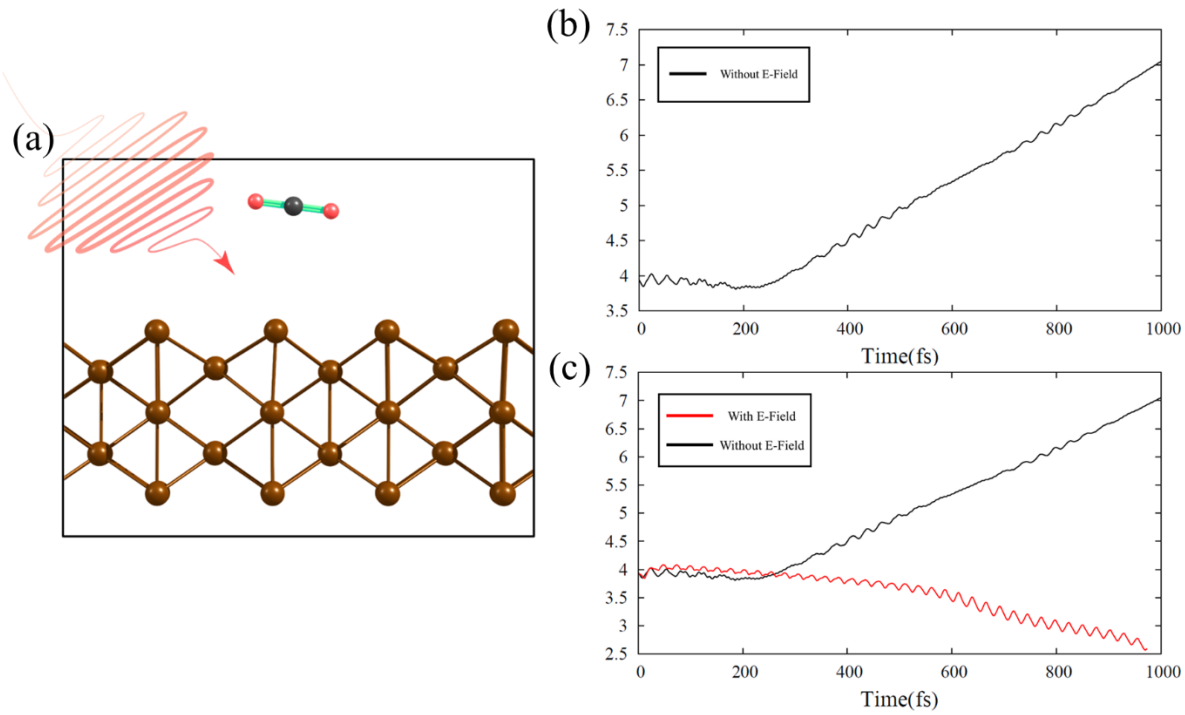

Figure 5-8. (a) The schematic configuration for carbon dioxide on Cu (110) surface with light pulse. (b) The trajectory of C-Cu bond length without external light field, and (c) with external light field (red line).

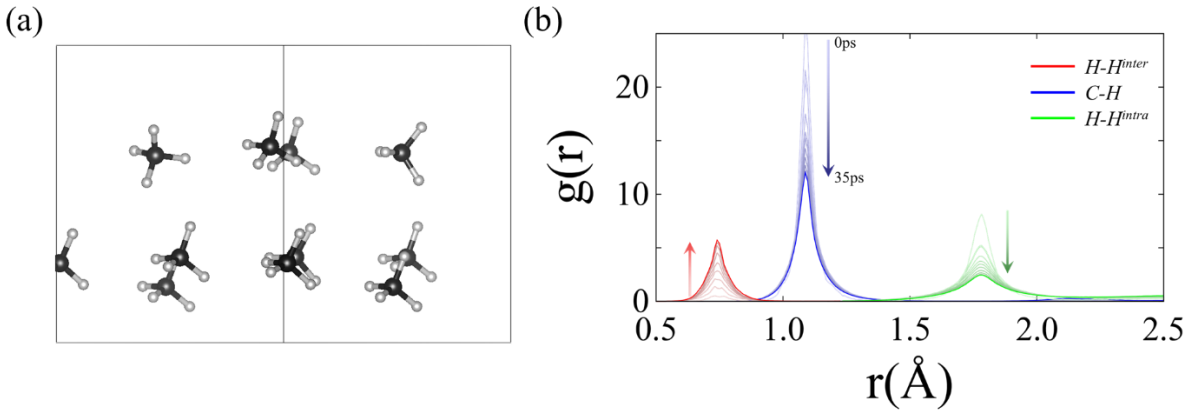

Figure 5-9. (a) The configuration of simulated super cell, and (b) the radial distribution function of inter-bonding of H-H (red line), intra-bonding of H-H (green line), and C-H bonding (blue line). The gradation, faint to deep, indicates the time flow from 0ps to 35ps.

5.7. Conclusion

In this part, the effect of harmonic or anharmonic frequency on the chemical reaction is investigated. The resonant phenomena can be driven by the harmonic frequency laser pulse, and this resonance can substitute the previous process or help to overcome a reaction barrier. The laser pulse with single harmonic frequency of O-C-O bending mode of carbon dioxide amplifies the scissoring motion of carbon dioxide, and this activation aims to the adsorbing the carbon dioxide molecule on a catalytic surface such as Cu (110). For the methane case, there is one more factor for effective resonance, anharmonicity. When the light pulse with single harmonic frequency is applied, the C-H bond is oscillating with envelope wave form. From this envelope wave form, another frequency can be calculated by Fourier transform of the trajectory of C-H bonding. The obtained frequency is interpreted to an anharmonic frequency. The effect of this anharmonic frequency is remarkable to amplify the C-H stretch mode. As Figure 5-7 depicted, the maximum displacement of C-H length with combination of harmonic and anharmonic frequency shows more five time higher than that with single harmonic frequency within a limited real amplitude of laser pulse. This effective amplification of C-H bonding aims to activate the methane molecule with weak laser pulse. The Ehrenfest dynamics simulation demonstrates that the laser pulse can generate the hydrogen molecules from liquid state methane at the room temperature. From these results, the resonance phenomena can aim to occur chemical reactions, and anharmonicity should be considered to effective reaction.

VI. Summary

In this thesis, the theoretical background to density functional theory (DFT), real-time time-dependent density functional theory (TDDFT), Ehrenfest dynamics, and molecular dynamics are introduced at the front part (II), and the hydrogen evolution reaction (HER) and oxygen reduction reaction (ORR) with catalyst system are handled at the middle part (III and IV). In the part III and IV, several catalysts are suggested for the HER and ORR processes, and the detailed mechanisms are different for each catalytic system. In these parts, the reactions are based on the electrochemical mechanism. Because of this base, there is a limitation to select proper catalyst for a chemical reaction. After understanding the mechanism of HER and ORR with catalyst, the novel mechanism using an external vector potential is suggested to overcome and substitute the catalysis system (V). In the part V, it is confirmed that the laser pulse aims to activate various molecules based on selective energy transfer method. [31, 37] The detailed mechanism is also investigated by analyzing the potential energy surface and classical model calculation. To amplify the selected vibration mode effectively, the anharmonicity is also considered. Remarkably, the effect of anharmonic frequency is amplified the vibration mode more five times higher than the effect of single harmonic frequency case. Herein, though the carbon dioxide and methane are targeted to substitute the traditional mechanism by using laser pulse, this laser pulse driven molecular activation can aim to overcome various restricted reactions with simple condition, or weak field.

VII. References

[1] J. J. Sakurai and J. Napolitano, *Modern quantum mechanics*, 2nd ed. Boston: Addison-Wesley, 2011, pp. xviii, 550 p.

[2] W. Kohn and L. J. Sham, "Self-Consistent Equations Including Exchange and Correlation Effects," *Phys. Rev.,* 140, no. 4A, pp. 1133-&, 1965.

[3] G. F. Bertsch, J. I. Iwata, A. Rubio, and K. Yabana, "Real-space, real-time method for the dielectric function," *Phys. Rev. B,* 62, no. 12, pp. 7998-8002, 2000.

[4] O. Sugino and Y. Miyamoto, "Density-functional approach to electron dynamics: Stable simulation under a self-consistent field," *Phys. Rev. B,* 59, no. 4, pp. 2579-2586, 1999.

[5] G. Nam, J. Park, M. Choi, P. Oh, S. Park, M. G. Kim, N. Park, J. Cho and J. S. Lee, "Carbon-Coated Core-Shell Fe-Cu Nanoparticles as Highly Active and Durable Electrocatalysts for a Zn-Air Battery", *ACS Nano, 9, no. 6, pp. 6493-6501,* 2015

[6] Y. Jeon, M. Choi, H. J. Choi, S. M. Jung, M. J. Kim, J. M. Seo, S. Y. Bae, S. Yoo, G. Kim, H. Y. Jeong, N. Park and J. B. Baek, "Antimony-doped graphene nanoplates", *Nature Communications,* 6, 7123, 2015

[7] Y. Kim, D. H. K. Jackson, D. Lee, M. Choi, T. W. Kim, S. Y. Jeong, H. J. Chae, H. W. Kim, N. Park, H. Chang, T. F. Kuech and H. J. Kim, "In Situ Electrochemical Activation of Atomic Layer Deposition Coated MoS2 Basal Planes for Efficient Hydrogen Evolution Reaction", *Advanced Functional Materials,* 27, 1701825, 2017

[8] Y. Yoon, A. Tiwari, M. Lee, M. Choi, W. Song, J. Im, T. Zyung, H. K. Jung, S. K. Lee, S. Jeon, and K. S. An, "Enhanced Electrocatalytic Activity by Chemical Nitridation of 2D Titanium Carbide MXene for Hydrogen Evolution", *Journal of Material Chemistry A* 6, 20869, 2018

[9] P. Hohenberg and W. Kohn, "Inhomogeneous Electron Gas," *Phys. Rev. B,* 136, no. 3B, pp. B864-&, 1964.

[10] J. P. Perdew and A. Zunger, "Self-Interaction Correction to Density-Functional Approximations for Many-Electron Systems," *Phys. Rev. B,* 23, no. 10, p. 5048, 1981.

[11] J. P. Perdew, K. Burke, and M. Ernzerhof, "Generalized gradient approximation made simple," *Phys. Rev. Lett.,* 77, no. 18, pp. 3865-3868, 1996.

[12] L. Hedin, "New Method for Calculating 1-Particle Greens Function with Application to Electron-Gas Problem," *Phys. Rev.,* 139, p. A796, 1965.

[13] F. Lechermann, L. Boehnke, D. Grieger, and C. Piefke, "Electron correlation and magnetism at the LaAlO3/SrTiO3 interface: A DFT plus DMFT investigation," *Phys. Rev. B,* 90, no. 8, p. 085125, 2014.

[14] G. Kresse and J. Furthmuller, "Efficient iterative schemes for ab initio total-energy calculations using a plane-wave basis set," *Phys. Rev. B,* 54, no. 16, pp. 11169-11186, 1996.

[15] P. Giannozzi *et al.,* "QUANTUM ESPRESSO: a modular and open-source software project for quantum simulations of materials," *J. Phys-Condens. Mat.,* 21, no. 39, p. 395502, 2009.

[16] X. Andrade *et al.,* "Real-space grids and the Octopus code as tools for the development of new simulation approaches for electronic systems," *Phys. Chem. Chem. Phys.,* 17, no. 47, p. 31371, 2015.

[17] D. Vanderbilt, "Soft Self-Consistent Pseudopotentials in a Generalized Eigenvalue Formalism," *Physical Review B,* 41, no. 11, pp. 7892-7895, 1990.

[18] G. Henkelman and H. Jónsson, A climbing image nudged elastic band method for finding saddle points and minimum energy paths, *J. Chem. Phys.* 113, 9901-9904 (2000)

[19] G. Henkelman and H. Jónsson, Improved tangent estimate in the nudged elastic band method for finding minimum energy paths and saddle points, *J. Chem. Phys.* 113, 9978-9985 (2000)

[20] Y. Zheng, Y. Jian, A. Vasileff, and S. Z. Qiao, "The Hydrogen Evolution Reaction in Alkaline Solution: From Theory, Single Crystal Models, to Practical Electrocatalysts", *Angew. Chem. Int. Ed.* 57, no. 26, pp. 7568-7579. 2018

[21] E. Runge and E. K. U. Gross, "Density-Functional Theory for Time-Dependent Systems," *Phys. Rev. Lett.,* 52, no. 12, p. 997, 1984.

[22] D. Shin, G. Lee, Y. Miyamoto, and N. Park, "Real-Time Propagation via Time-Dependent

Density Functional Theory Plus the Hubbard U Potential for Electron−Atom Coupled Dynamics Involving Charge Transfer," *J. Chem. Theory Comput.*, 12, pp. 201-208, 2016.

[23] A. Castro *et al.*, "octopus: a tool for the application of time-dependent density functional theory," *Phys. Status. Solidi. B*, 243, no. 11, pp. 2465-2488, 2006.

[24] R. M. Martin, *Electronic structure : basic theory and practical methods*, 1st pbk. ed. Cambridge, UK ; New York: Cambridge University Press, 2008, pp. xxii, 624 p.

[25] J. K. Norskov, J. Rossmeisl, A. Logadottir, L. Lindqvist, J. R. Kitchin, T. Bligaard, and H. Jonsson, "Origin of the Overpotential for Oxygen Reduction Reaction at a Fuel-Cell cathode", *J. Phys. Chem. B.*, 108, no. 46, pp. 178866-17892, 2004

[26] E. Beaurepaire, J.-C. Merle, A. Daunois, and J.-Y. Bigot, "Ultrafast Spin Dynamics in Ferromagnetic Nickel", *Phys. Rev. Lett.*, 76, no. 22, pp. 4250-4253, 1996

[27] C. D. Stanciu, F. Hansteen, A. V. Kimel, A. Kirilyuk, A. Tsukamoto, A. Itoh, and Th. Rasing, "All-Optical Magnetic Recording with Circularly Polarized Light", *Phys. Rev. Lett.*, 99, no. 4, pp. 047601, 2007

[28] A. R. Khorsand, M. Savoini, A. Kirilyuk, A. V. Kimel, A. Tsukamono, A. Itho, and Th. Rasing, "Role of Magnetic Circular Dichroism in All-Optical Magnetic Recording", *Phys. Rev. Lett.*, 108, no. 12, pp. 127205, 2012

[29] X.-J. Chen, "Fundamental mechanism for all-optical helicity-dependent switching of magnetization", *Scientific Reports*, 24, no. 7, pp. 41294, 2017

[30] G. Kichin, M. Hehn, J. Gorchon, G. Malinowski, J. Hohlfeld, and S. Mangin, "From Multiple- to Single-Pulse All-Optical Helicity-Dependent Switching in Ferromagnetic Co/Pt Multilayers", *Phys. Rev. Lett.*, 12, no. 2, pp. 024019, 2019

[31] P. M. Hundt, B. Jiang, M. E. van Reijzen, H. Guo, and R. D. Beck, "Vibrational Promoted Dissociation of Water on Ni (111)", *Science*, 344, no. 6183, pp. 504-507, 2014

[32] B. Jiang and H. Guo, "Communication: Enhanced dissociation chemisorption of CO2 via vibrational excitation", *J. Chem. Phys.*, 144, pp. 091101, 2016

[33] R. J. Levis, G. M. Menkir, and H. Rabitz, "Selective Bond Dissociation and Rearrangement with Optimally Tailored, Strong-Field Laser Pulse", Science, 292, no. 5517, pp. 709-713, 2001

[34] S. Wang, "Efficiently Calculating Anharmonic Frequencies of Molecular Vibration by Molecular Dynamics Trajectory Analysis", *ACS Omega*, 4, no. 5, pp. 9271-9283, 2019

[35] I. Morichika, K. Murata, A. Sakurai, and S. Ashihara, "Molecular ground-state dissociation in the condensed phase employing plasmonic field enhancement of chirped mid-infrared pulses", *Nature Communications*, 10, pp. 3893, 2019

[36] Y. Zheng, W. Zhang, Y. Li, J. Chen, B. Yu, J. Wang, L. Zhang, and J. Zhang, "Energy related CO2 conversion and utilization: Advanced materials/nanomaterials, reaction mechanism and technologies", *Nano Energy*, 40, pp. 512-539, 2017

[37] Y. Choi, Y. Park, T. Kang, and L. P. Lee, "Selective and sensitive detection of metal ions by plasmonic resonance energy transfer-based nanospectroscopy", *Nature Nanotech.*, 4, pp. 742-746, 2009

VIII. Acknowledgements

2009년 유니스트에 입학한 후부터 2021년 박사학위를 받는 때까지 정말 많은 박사님과 교수님들의 도움을 받았습니다. 먼저 저에게 학문적으로 그리고 연구적으로 가장 큰 가르침을 주신 박노정 교수님께 감사드립니다. 교수님께서 연구를 하실 때 임하시는 진지함과 열정을 옆에서 보고 배우며, 저 또한 연구자로써 가져야할 마음가짐에 대해 깊게 생각해보고 진지하게 연구에 몰두할 수 있도록 방향을 제시해주시고 도와 주셨습니다. 항상 연구에 대해 고민하시고 생각하시는 모습을 늘 깊이 생각하고, 본받을 수 있도록 노력하며 성장하겠습니다. 제가 제일 처음 연구실이라는 곳을 접하고 학부생 인턴으로서 연구활동이라는 것을 시작할 수 있도록 도와 주신 서울대학교 이규태 교수님께도 감사의 인사를 드립니다. 비록 지금의 분야와는 다르지만 연구활동을 처음 접하고, 연구의 즐거움과 중요성, 그리고 연구를 바라보는 눈을 알려주셔서 감사드립니다. 무기화학적 배경지식을 튼튼히 쌓을 수 있도록 훌륭한 강의를 해 주신 나명수 교수님, 문회리 교수님께도 감사의 말씀을 드립니다. 항상 새로운 연구 주제로 디스커션을 해주시고 많은 것을 알려주신 인천대학교 김정우 교수님께도 감사드립니다. 3년의 기간동안 학교 연구실을 벗어나 한국화학연구원이라는 정출연에서 일하는 동안 많은 실무적인 가르침을 주신 장현주 센터장님, 임진오 박사님, 김현우 박사님, 이예리 박사님, 장승훈 박사님께도 감사드립니다. 학교에서 배우고 연구한 내용들이 실제 연구소에서 어떻게 적용되고 활용 가능한지 배울 수 있는 소중한 시간이었습니다. 또한, 좋은 연구 내용이 있을 때 소개해주시고 추천해주시는 김현우 박사님께 감사드립니다. 박사학위 심사를 맡아 주신 박형렬 교수님, 이준희 교수님, 이근식 교수님, 그리고 김현우 박사님에게 감사합니다. 연구실에서 동고동락하며 도움을 많이 받은 신동빈 박사님과 김범섭 학생에게도 고맙습니다. 마지막으로 그동안 저를 길러 주시고 믿음으로 지지해주시는 부모님께 감사드립니다. 지면의 부족으로 미처 다 전하지 못 하였지만, 저를 이끌어 주시고 가르침을 주신 많은 교수님들과 박사님들에게 진심으로 감사의 말씀을 드립니다.